Mechanical Engineering Advances 2025, 3(3), 3077.
https://doi.org/10.59400/mea3077

Article

Development of a stealth-enabled supersonic interceptor missile: Design, propulsion, and guidance

Jacob Nagler

Nagler Independent Research Center, Haifa 3478403, Israel; Jacobyan123@gmail.com

CITATION

Nagler J. Development of a stealth-enabled supersonic interceptor missile: Design, propulsion, and guidance. Mechanical Engineering Advances. 2025; 3(3): 3077. https://doi.org/10.59400/mea3077

ARTICLE INFO

Received: 9 April 2025
Revised: 9 June 2025
Accepted: 12 June 2025
Available online: 12 August 2025

Abstract: This research presents the Horned-Viper project—a technological demonstrator for a stealth-enabled, supersonic homing interceptor missile with multi-domain engagement capability (air-to-air, air-to-ground, and ground-to-ground). Distinguished by a dual-horn inlet blended into the fuselage, Horned-Viper achieves a 45% reduction in frontal RCS compared to canonical designs (e.g., AIM-120C-7, R-73). Its two-stage, dual-pulse solid-propellant architecture delivers a total impulse of 538.6 kN·s while sustaining 10 g maneuvers at Mach 1.5 and achieving a 60 km range from a 6000 m altitude launch—exceeding comparable systems by 20%–30% in agility and thrust management. A refined PNG-based guidance loop, augmented with PID (proportional-integral-derivative)-controlled canards, ensures a 10 Hz closed-loop bandwidth, yielding a 12% shorter time-to-kill relative to AIM-120C-7 under identical intercept conditions. The warhead employs directional spherical fragments, maximizing lethality within a 10 m lethal radius with an optimized fragment mass-to-explosive ratio, surpassing traditional fragmentation yields by 15 %. High-fidelity CFD (ANSYS Fluent) and 6-DOF trajectory simulations validate aerodynamic shaping and flight stability, demonstrating drag coefficient minimization in the Mach 1.8–2.2 regime and lift-to-drag improvements of 25% during terminal maneuvers. Collectively, these quantitative advances—coupled with modular servomotor and warhead innovations—establish Horned-Viper as a promising next-generation interceptor concept with critical performance advantages over X-90, R-73, Sidewinder, and Arrow systems.

Keywords: solid propellant; rocket motor; booster; dual-pulse; anti-radar; stealth; camouflage; interceptor missile; PID

1. Introduction

The Horned-Viper project is presented explicitly as a technological demonstrator. Its primary aim is to validate and integrate novel design elements—stealth geometry, dual-pulse solid propulsion, high-agility control surfaces, and a directed-fragmentation warhead—within a unified interceptor architecture. Although informed by academic and educational design methodologies, Horned-Viper transcends a purely pedagogical exercise by pursuing near-operational fidelity through high-fidelity simulations, proposed wind-tunnel validation, and subscale flight tests.

1.1. Background and motivation

While student missile projects have offered valuable educational experiences in propulsion, guidance, and structural design, they typically focus on isolated subsystems and culminate in small-scale tests. In contrast, defense research has prioritized incremental improvements to existing platforms like the Sidewinder or AIM-120. Despite progress in both domains, no prior academic or student-led effort has successfully integrated a stealth-optimized airframe, dual-pulse propulsion, high-

agility control, and a directional fragmentation warhead into one coherent interceptor design.

The Horned-Viper project fills this gap by serving as a true technological demonstrator—not just an educational model. It unifies advanced stealth geometry, a two-stage dual-pulse solid motor, PID-controlled canard-tail actuation, and an optimized warhead into a single, simulation-validated system. Unlike earlier academic efforts in Israel (e.g., SELA, CANAAN, Sky Fox), which emphasized individual innovations, Horned-Viper demonstrates how these elements can be engineered to work together in a next-generation, multi-role interceptor concept with realistic operational potential.

1.2. Literature review

Fitzpatrick [1], inspired by the Sidewinder air-to-air missile family, outlined its developmental and operational advancements, highlighting its modular structure—comprising guidance, control, and arming components—and its affordability (approximately $70,000 per unit in the 1980s). These models demonstrated diverse aerodynamic capabilities and significantly influenced both military and academic research.

In 1990, Cal Poly Pomona initiated the Long-Range Air-Launched Weapon (LAW) project [2], aiming to deliver a 740.8 km range from an aircraft flying at Mach 0.6–0.7 and altitudes between 30,000 and 35,000 ft. The design incorporated composite materials, reducing the overall weight by 50%, achieving a total mass of 762 kg, including a 136 kg avionics and payload system. A proximity fuse enabled target detection within 100 ft. In 1998, the University of Cincinnati developed a two-stage sounding rocket [3] using Nike and Orion surplus motors to study zero-gravity attitude control. The project included sequence, vibration, and spin balance testing. The University of Alabama in Huntsville (UAH) conducted a 2003 comparative analysis of solid propellant and turbojet systems [4]. Concurrently, practical applications for aerial and ground-based propulsion were demonstrated by various U.S. defense contractors [5–8]. Among them, Foster et al. [7] advanced techniques for vacuum specific impulse computation, 3D grain optimization using genetic algorithms, and combustion instability analysis. Their comprehensive work extended to ramjet and scramjet propulsion, including experimental diagnostics via laser-induced fluorescence.

Numerous hybrid-sounding rocket projects have since emerged [9–24]. For instance, Okninski et al. [15] and the Warsaw University of Technology developed the "Amelia" series, which included a reusable SRM, a two-pulse SRM, and a Rotating Detonation Engine prototype [20]. Nicholson et al. [16] designed a hybrid system combining solid and liquid propulsion, while Apel et al. [17] introduced the "AQUASONIC" hybrid rocket using nitrous oxide and polyethylene, achieving Mach 1.05 and altitudes up to 6 km. The HYCOM engine test facility introduced by Lesttrade et al. [18] featured modular configurations for combustion chamber geometry and injector systems, with instrumentation including ultrasonic sensors and X-ray diagnostics. Bach et al. [19] developed the MIRA LOX-ethanol engine, pressurized to 250 bar. Ganesh et al. [21] designed a subsonic cruise missile (Mach 0.8) using

historical wing configurations. Nowakowski et al. [22] developed the "H1" supersonic SRM as part of the ILR-33 "Amber" project. Dutaa et al. [23] introduced the "Yellow-Jacket" series with liquid engines, while Heeg et al. [24] contributed the HYDRA hybrid system to the Faust rocket program. Additionally, Nagineni and Deepika [25] conducted a CFD-based performance evaluation of conical and bell-shaped nozzles after reviewing multiple nozzle types. Now, a brief comparison between literature references will be presented in the context of missile main parameters performance.

Fitzpatrick [1] details a versatile solid-propellant air-launched weapon achieving Mach 2.5, optimized for short-to medium-range engagement (0.6–22 miles), while Basciano [2] describes a long-range interceptor with a combined rocket-ramjet system, extending reach up to 400 nautical miles and prioritizing high-altitude performance. The latter's composite airframe reduces weight by 50%, contrasting with Ref. [1]'s more compact 70–89 kg system. In contrast to these airborne systems, Bouchez [3] and Paul et al. [5] focus on ground-based or vertical launch designs. Bouchez [3] employs a two-stage sounding rocket using surplus Nike and Orion motors for microgravity research, while Paul et al. [5] explore a high-thrust guided missile designed for rotary-wing and vehicle defense, reaching Mach 2 with a 297 kg mass. Several designs, including [6,9,10], explore hybrid propulsion. Neu et al. [6] use nitrous oxide and HTPB in a titanium tank to achieve a thrust of 2492 N, while Dyer et al. [9] report thrusts exceeding 1 MN in large-scale sounding rockets. Grosse and Schlatzke [10] emphasize tactical deployment, with a small-scale 8 km range hybrid system using $AlMg_3$ oxidizer and paraffin/HTPB fuel. High-efficiency oxidizers like H_2O_2 and N_2O are employed in [11,13], respectively. Tsohas et al. [11] utilize a five-port grain and carbon composite structure for moderate thrust (4 kN), while Ronningen et al. [13] achieve a 12 km apogee with an N_2O/HTPB configuration and carbon-fiber airframe. Reusable and student-designed systems, such as those in [12,14,15], prioritize cost-effective construction. Tran et al. [14] achieves a 7.6 km apogee using paraffin/HTPB with an Isp of 205 s, while the Amelia series in [15] demonstrates Mach 2.7 performance through composite SRMs and prototype rotating detonation engines. Several studies, such as [16–19] investigate advanced hybrid and liquid propulsion systems. Apel et al. [17] reaches Mach 1.05 with a polyethylene/N_2O hybrid, while [19] introduces a green LOX-ethanol liquid engine producing 500 N thrust. Lestrade et al. [18] complements these with modular hybrid engine testbeds for academic validation. Long-range cruise and supersonic interceptor designs are evident in [21] and [22]. Ganesh et al. [21] details a subsonic cruise missile with a 1500 km range, while Nowakowski et al. [22] introduces the H1 supersonic SRM capable of Mach 3 and 6000 N thrust. ILR-33 Amber, also under [22], pushes to Mach 4 and 100 km altitude, demonstrating hybrid propulsion scalability. Full-scale development is reflected in [23] with a 15 kN LOX-kerosene engine for supersonic flight and in [24] with the Faust hybrid rocket achieving a 5.4 km apogee at modest thrust levels, suitable for educational and experimental applications. This comparison illustrates how different platforms balance thrust, range, altitude, and propulsion strategy based on mission constraints, from lightweight academic testbeds to high-speed interceptors and tactical defense systems.

Israeli academic and defense institutions have also contributed significantly. The SELA supersonic missile (Mach 1.5 at sea level) was introduced in 2004 by Perelstein

et al. [26]. Sivan et al. [27] proposed the subsonic, medium-range "CANAAN" in 2009, designed for low radar observability and penetration of reinforced structures. In 2012, the "Sky Fox" ramjet interceptor—a conceptual predecessor to the current Horned Viper project—was introduced, featuring a hexagonal star grain and directional warhead with 7500 tungsten fragments [28]. Achache et al. [29] designed the "Parash" anti-tank missile with dual SRMs and a 4.1 km range. The evolution of these projects is illustrated in **Figure 1** and the Appendix. The Horned Viper project [28] is the latest initiative, proposing a homing, supersonic interceptor with stealth capabilities. It integrates dual star-grain SRMs (including a booster), iron-sphere-based warheads, and a modified guidance system.

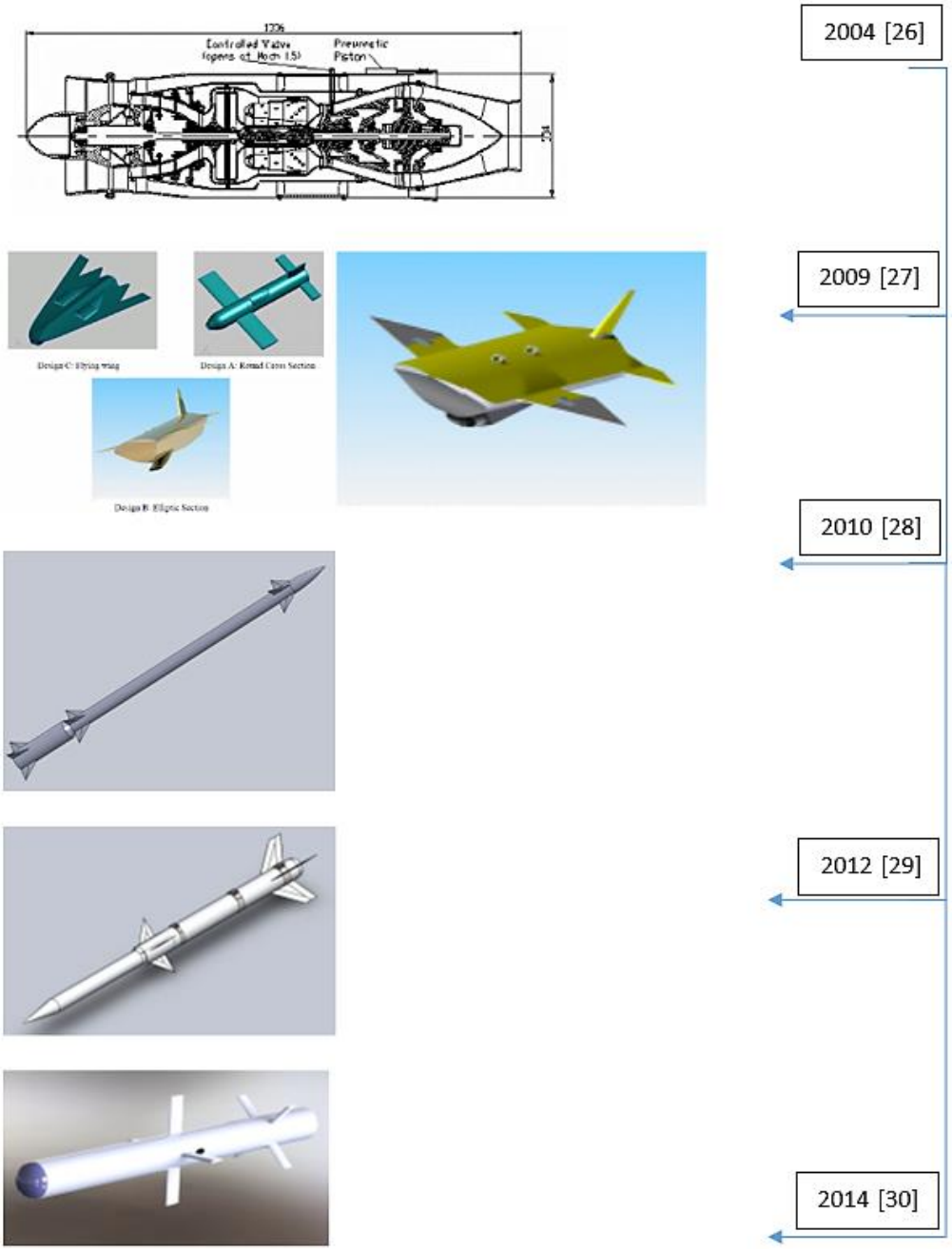

Figure 1. Israeli prototype UG missiles evolution.

Broad academic reviews by Krishnan [30] and Cavney [31] have examined student-led trends in rocketry, including regression rate enhancement through propellant additives, hybrid ignition methods, nozzle geometry design, and insulation strategies. Okninski [32,33] has explored hybrid propulsion applications for suborbital and space transport missions, emphasizing the use of safe and efficient oxidizers such as LOX, N_2O, NYTROX, and HTP. Hybrid configurations such as LOX/HTPB, N_2O/polymer-based fuels, and NYTROX/paraffin wax have shown promise under logistical constraints. Notably, studies on multi-port fuel grains, booster integration, and extended burn durations further validate hybrid propulsion as a viable high-performance solution.

1.3. Main challenge design parameters and components

The performance parameters are (i) total impulse (Isp [sec]), which measures the total thrust produced per unit of propellant expended. Higher Isp means greater efficiency and potentially higher payload capacity. (ii) Thrust [kN] represents the maximum force generated by the motor. Higher thrust allows for faster acceleration and potentially reaching higher altitudes. (iii) Burn Time [seconds] represents the duration of the motor's thrust generation. Longer burn times can achieve higher velocities but may require additional complexity. However, the main design parameters are (i) propellant type, which might be solid, liquid, or hybrid fuels, each with its own advantages and challenges. (ii) Chamber pressure [MPa] inside the combustion chamber. Higher pressure can lead to greater thrust but requires stronger materials and more complex design. (iii) Motor geometry includes factors like diameter, length, and nozzle configuration. These influence performance and manufacturability. (iv) Material selection represents the materials used for the chamber, nozzle, and casing impact weight, strength, and cost.

The safety parameters include (i) Estimated Impulse Safety Factor (ISF), which measures the motor's ability to withstand unexpected pressure spikes. A higher ISF indicates a safer design. (ii) Grain geometry (solid propellants) represents a specific configuration of the propellant grain and can influence burn rate and stability.

Additional considerations were (i) Cost of materials and manufacturing. (ii) Manufacturability represents the complexity of the design. Especially, fabrication has also been considered. (iii) Scalability represents the potential for the design to be scaled up for larger applications.

The configuration design includes the following four main components: (i) Aerodynamic Configuration: The missile features a canard-controlled aerodynamic configuration with freely rotating tails. Detailed geometry and position design of the fins are verified through tunnel experiments. The missile's aerodynamic performance is analyzed using Computational Fluid Dynamics (CFD) simulations. (ii) Propulsion System: The propulsion system consists of two solid propellant star grain motors arranged in a two-stage configuration. The first stage acts as a booster, providing initial acceleration, while the second stage operates in two pulses for optimal thrust management. The propellant composition includes HTPB as a binder, AP as the oxidizer, and aluminum as a metallic supplement. (iii) Guidance system: The guidance system employs proportional navigation with an onboard inertial measurement unit

(IMU) and GPS. Servo motors and a PID controller ensure accurate canard deflection. (iv) Warhead Design: The warhead consists of spherical iron fragments propelled by high-explosive detonation. Fragmentation velocity and distribution are calculated using Gurney equations, with a proximity fuse detonator for maximum lethality.

Accordingly, the main missile conceptual design topics are derived in each design stage (SRR, PDR, and CDR) as: (i) design requirements; (ii) missile aerodynamics; (iii) guidance system; (iv) warhead; (v) flight control systems; (vi) propulsion system; (vii) structural parts and choice of materials.

Table 1. PDR Aerodynamic configurations comparison—Thrust steering\wing\canard\tail or their combination.

Thrust Maneuvering Control Type	Advantages	Disadvantages	Schematic
Canard	Location and simple integration with subsystems. Increased lift for a statically stable missile. Quick maneuvering response.	Stall at high angles of attack, problematic lifting in roll—rudder saturation. The canard configuration produces a large induced roll. Note: Sometimes a canard configuration requires a larger tail for static stability.	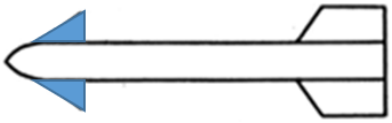
Tail	Small axis moments. A small induced roll (tail wrestling phenomenon). Good steering efficiency—flow stream flow. Clean, great steering wheel range.	Slow, opposite lift force, far from electronics. The actuators occupy a volume around the "hot part".	
Trailing Edge Flap	Optimize lift and control for reduced takeoff distances and decreased approach speeds.	Effectiveness decreases as the aircraft accelerates and reaches higher speeds during cruise phases due to increased induced drag. Trailing edge flaps compatibility adds weight and complexity to an aircraft's structure (lightweight composite material is required to use). Design engineering and integration complex. High maintenance and wear inspection cycles. Increased noise levels during landing and takeoff.	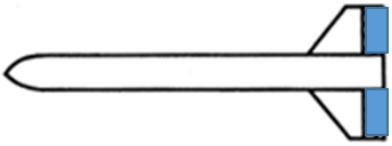
Moving Wing	Very fast maneuvering response.	Large axis moments require large actuators. High sensitivity to changes in the center of gravity location. Large wings (high induced roll and drag). Storage in a container is problematic.	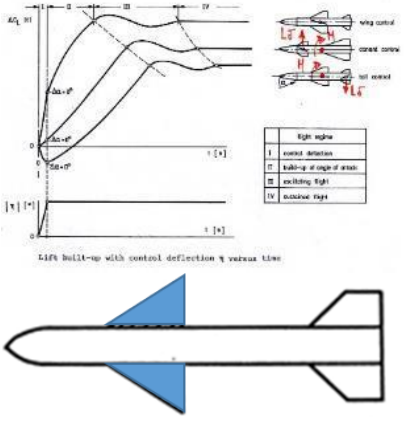

The PDR step design includes alternatives in each of the following content areas: aerodynamics of the missile (see **Table 1**), guidance system, homing head section, flight control systems, the propulsion system, and structural parts together with materials selection. The CDR stage continuing destinations include: (i) Selecting a final configuration in each of the design areas and a general final configuration. (ii) Carrying out an in-depth

design of each of the listed assemblies. (iii) Conducting tunnel experiments for the purpose of verifying aerodynamic coefficients. (iv) System Design.

2. System requirements

The missile system's main requirements are elaborated as follows: (i) Maximum range—140 km. (ii) Warhead mass—20 kg. (iii) Target maximum speed—2 Mach. (iv) Maximum maneuver—10 g. (v) Anti-radar capability. The general initial missile assembly concept is exhibited in **Figure 2**.

Figure 2. General initial missile assembly concept.

3. Aerodynamics computational analysis and flight testing

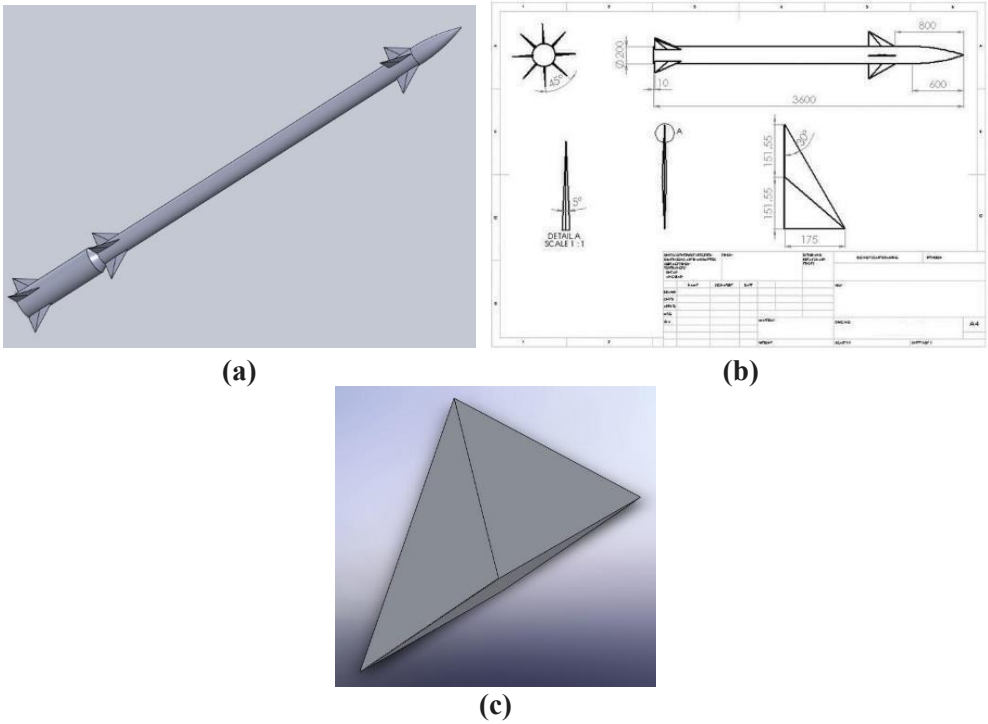

(a) **(b)**

(c)

Figure 3. Suggested initial missile aerodynamic configuration: **(a)** Schematic 3D illustration; **(b)** Initial aerodynamic drawing illustration; **(c)** Fin 3D illustration.

In its terminal flight phase (M = 1.5), the interceptor (initial model presented in **Figure 3**) must sustain a minimum aerodynamic load factor of n = 10. Likewise, at an operational altitude of 6000 m and Mach 1.5, the design range objective is 60 km ± 10% from launch. During Preliminary Design Review (PDR), we evaluated several controls—aerodynamic configurations—thrust vectoring, wing deflection, canards,

tail surfaces (**Table 1**), and their combinations—using initial drag and load-factor predictions derived from **Figures 4** and **5**. The optimum solution combined rearward-tilting canards with a tilting tail plane, achieving the target performance at an angle of attack (α) of 10° and a canard deflection (δ) of 10°.

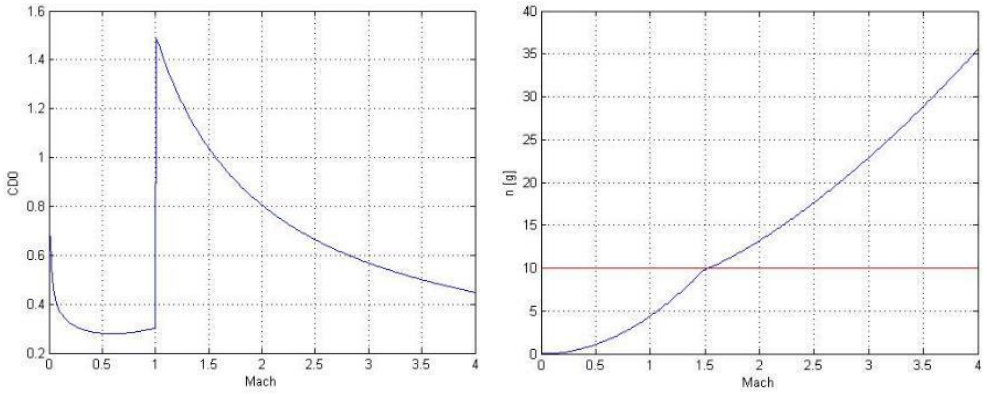

(a) **(b)**

Figure 4. Suggested initial missile aerodynamic configuration: **(a)** Selected aerodynamic configuration versus drag model; **(b)** Mach number variations versus load factor.

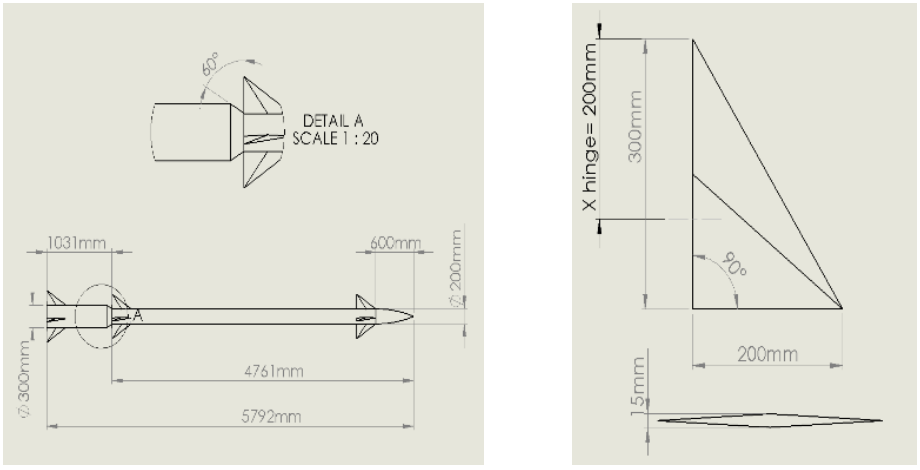

(a) **(b)**

Figure 5. Accurate missile aerodynamic configuration: **(a)** Full selected aerodynamic configuration drawing; **(b)** Fin drawing.

At Critical Design Review (CDR), our aerodynamic objectives were refined to: (1) precisely define fin geometry and spatial placement relative to the center of gravity; (2) finalize missile body and ogive-nose contours; (3) validate predictions via wind-tunnel tests; (4) characterize high-altitude aerodynamic behavior; (5) specify a tangent-ogive nose with a length-to-diameter ratio of 3; (6) implement independent ± 40° canard actuation for pitch and roll control; (7) utilize freely rotating tail fins; (8) integrate a dual-pulse sustainer and booster propulsion system; (9) standardize fin and canard airfoil sections to a double-wedge profile (t/c = 5%); (10) position control-surface hinges at two-thirds of the root chord; (11) employ electric servo actuators for all control surfaces.

3.1. Aerodynamics computational analysis

The aerodynamic behavior of the Horned-Viper missile is evaluated using the classical force and moment relations, derived under steady, incompressible, or compressible flow assumptions depending on the Mach regime. The key aerodynamic quantities are expressed as:

$$\text{Lift Force: } L = \frac{1}{2}\rho v^2 C_L A \tag{1}$$

$$\text{Drag Force: } D = \frac{1}{2}\rho v^2 C_D A \tag{2}$$

$$\text{Pitching Moment: } D = \frac{1}{2}\rho v^2 C_M A c \tag{3}$$

$$\text{Normal Force: } N = \frac{1}{2}\rho v^2 C_N A \tag{4}$$

where $\rho, v, C_D, C_L, C_M, C_N, A, c$ are the air density, relative velocity of the missile with respect to the air $[m/s]$, the aerodynamic coefficients (drag, lift, pitching moment, and normal force coefficients), the reference planform area, and the characteristic length, typically the mean aerodynamic chord $[m]$, respectively.

These expressions form the basis for both analytical estimations and validation of numerical CFD (Computational Fluid Dynamics) results. The coefficients themselves are functions of Mach number, angle of attack (α), and control surface deflection (δ) and must be determined via simulation or experimental methods.

3.1.1. CFD simulation methodology

To obtain high-fidelity aerodynamic coefficients and flow characteristics, Computational Fluid Dynamics (CFD) simulations were conducted using ANSYS Fluent, with emphasis on transonic and supersonic regimes relevant to missile engagement scenarios. The simulation domain resolves the Reynolds-Averaged Navier–Stokes (RANS) equations for compressible, viscous flow. These are formulated as:

Continuity equation (mass conservation):

$$\frac{\partial \rho}{\partial t} + \nabla \cdot (\rho \vec{v}) = 0 \tag{5}$$

Momentum conservation:

$$\frac{\partial (\rho \vec{v})}{\partial t} + \nabla \cdot (\rho \vec{v}\vec{v}) = -\nabla p + \nabla \cdot \tau + \rho g \tag{6}$$

Energy conservation:

$$\frac{\partial (\rho E)}{\partial t} + \nabla \cdot [\vec{v}(\rho E + p)] = \nabla \cdot (k \nabla T) + \nabla \cdot (\tau \cdot \vec{v}) \tag{7}$$

where v, p, τ, E, T, k, g are the velocity vector, static pressure, viscous stress tensor, total energy per unit mass, temperature, thermal conductivity, and body force per unit mass, respectively.

The Shear Stress Transport (SST) k–ω model was employed to capture turbulence effects, particularly around control surfaces and sharp leading edges. This model

blends the robustness of the k–ε model in the free stream with the k–ω model's near-wall accuracy, making it suitable for high-speed, boundary-layer-dominated flows.

Boundary conditions include the following: (i) Freestream Inlet: Supersonic inflow at Mach 2.0, corresponding to standard atmospheric conditions at 6000 m. (ii) Pressure Outlet: Static ambient pressure for subsonic outflow zones. (iii) No-Slip Walls: Viscous boundary layer enforced on all missile surfaces. (iv) Adiabatic Wall: Thermal insulation assumed unless otherwise stated.

Mesh and convergence criteria include: (i) A structured and unstructured hybrid mesh was generated with inflation layers near walls to resolve the viscous sublayer ($y^+ < 1$). (ii) Mesh independence was confirmed through iterative refinement. (iii) Residuals were monitored for all conservation equations, with convergence set at 10^{-6} for continuity and momentum, and 10^{-8} for energy. (iv) Forces and moments were integrated over the surface using Fluent's post-processing tools to extract C_D, C_L, C_M and C_N.

3.1.2. Key findings from CFD and aerodynamics analytics results

As illustrated in **Figure 4**, the flow visualization confirms stable supersonic flow with shock structures anchored near the canard and tail fin leading edges. The following observations were made: (i) Shock wave interaction with control surfaces was minimized by tailoring surface deflection and fin placement, improving pitch stability, and reducing drag penalties. (ii) Optimal aerodynamic shaping resulted in drag coefficient minimization within the Mach 1.8–2.2 range. (iii) CFD-derived coefficients were used directly in 6-DOF trajectory simulations and validated against empirical data trends where available. (iv) The canard–tail combination yielded enhanced lift-to-drag ratios during maneuvering phases, contributing to sustained high-load turns at terminal speeds.

These CFD simulations underpin the missile's aerodynamic integrity and confirm that the Horned-Viper configuration is viable for both stability and agility under high-speed intercept conditions.

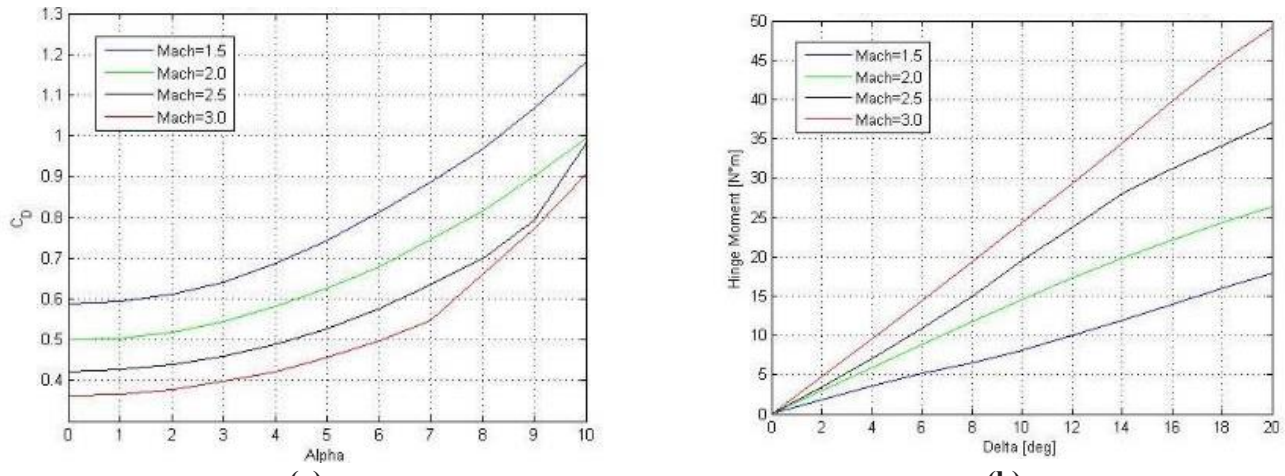

(a) **(b)**

Figure 6. Aerodynamic coefficients at altitude 6000 m: **(a)** Drag coefficient versus angle of attack; **(b)** Hinge moment versus canard deflection (δ) angle.

Moreover, **Figure 5** depicts the finalized aerodynamic missile geometry. **Figure 6a** plots the drag coefficient vs. α (reference area = 0.031 m^2; reference length = 0.20 m), showing a maximum (AOA—angle of attack) α of 10° before δ reaches its ±10° limit. **Figure 6b** and the hinge-moment curve in **Figure 7** confirm that α and δ remain within actuation limits ($|M_{hinge}| < 35$ N·m), establishing a maximum canard deflection of ±20°. Under trimmed flight conditions, the normal force coefficient (C_N) shown in **Figure 8** corresponds to a fully fueled mass of 218.8 kg (empty mass = 73.8 kg).

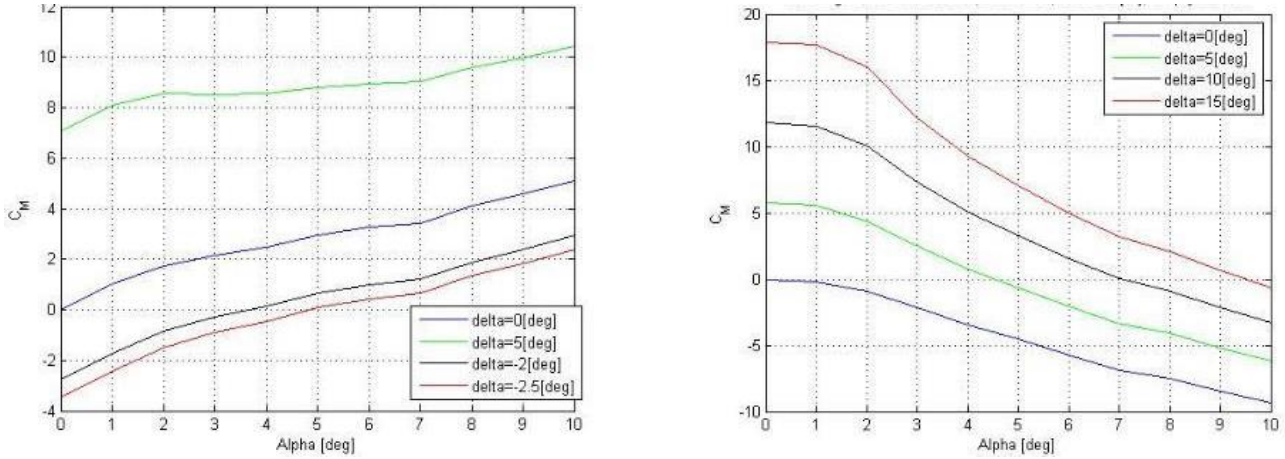

(a) **(b)**

Figure 7. Pitching moment coefficient versus (α) at M = 1.5 and Altitude = 6000 m for **(a)** Full missile case; and **(b)** Empty missile case.

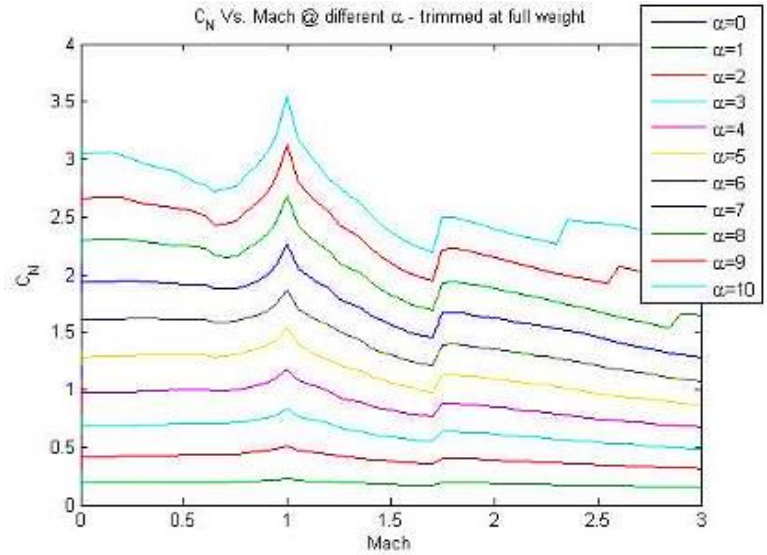

Figure 8. Normal coefficient versus M at different (α) angles for the full weight case.

The pitching-moment behavior (**Figure 7**) validates longitudinal stability across the operational α range. Time-history data in **Figure 9** indicate a total flight duration of 120 s for a 50° loft-launch trajectory: at 1200 m altitude the missile initiates a pitch-down maneuver, and by 6100 m it transitions into level, straight-and-steady flight.

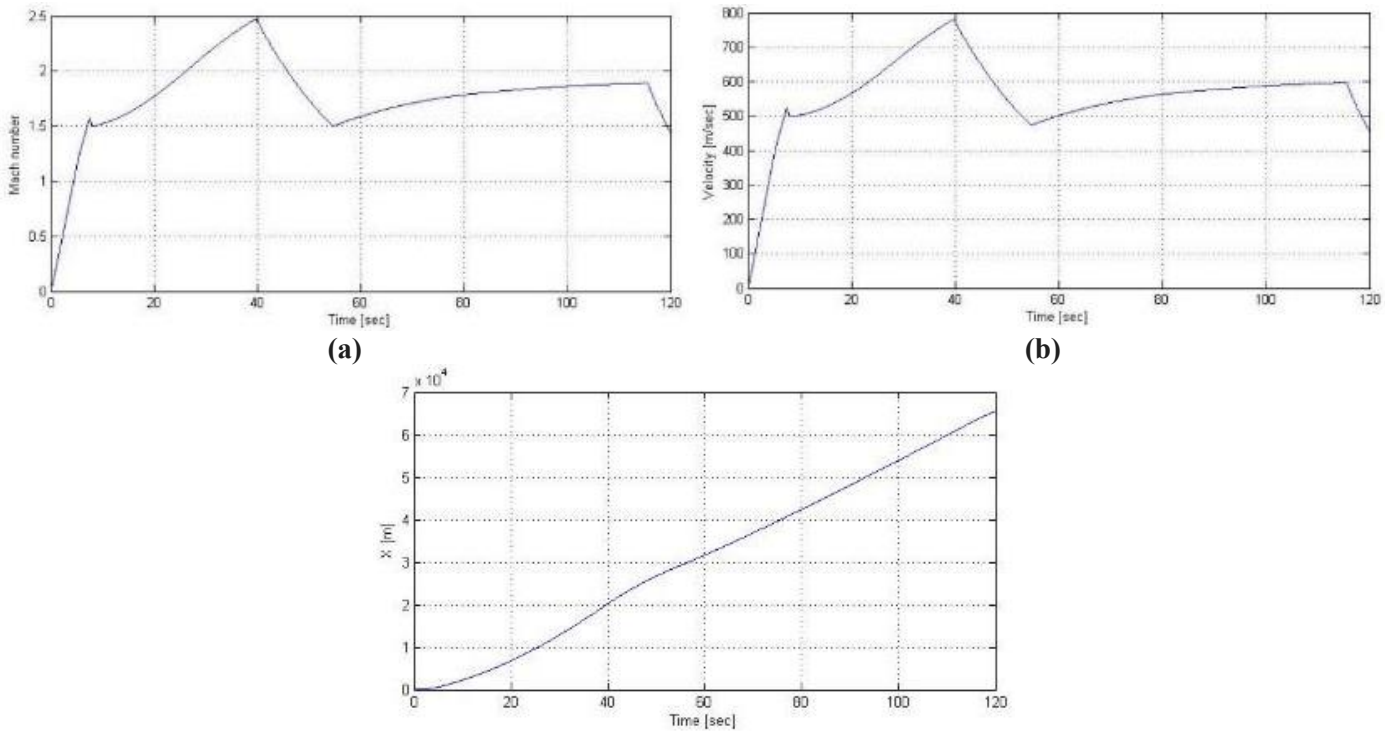

(a) **(b)** **(c)**

Figure 9. Missile performance parameters versus time: **(a)** Mach number; **(b)** Total velocity; **(c)** Range.

Finally, **Figure 10** illustrates maneuver performance: the achievable load factor increases monotonically with Mach number and angle of attack, though it is moderated by the vehicle's instantaneous mass. This trend underscores the trade-off between speed, agility, and fuel consumption in terminal engagements.

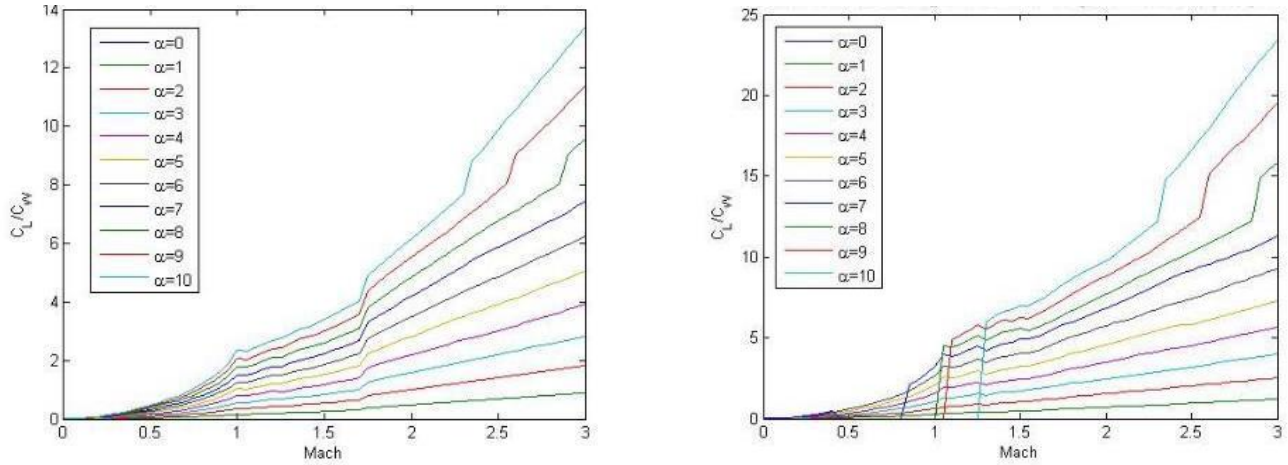

(a) **(b)**

Figure 10. 2nd stage trimmed: Load factor ratio versus M at different α angles for **(a)** Full weight; **(b)** Empty weight.

4. Propulsion system analysis and solid rocket motor (SRM) selection

During the Preliminary Design Review (PDR) phase, multiple propulsion architecture candidates were evaluated for their suitability in the Horned-Viper missile

platform. The alternatives are illustrated in **Figure 11**, which presents a comparative decision chart based on propellant mass efficiency and system complexity. The following four solid-propellant configurations were analyzed: (i) Single-stage. (ii) Dual-pulse single-stage motor. (iii) Two-stage rocket motor. (iv) Two-stage motor with a dual-pulse second stage. Each configuration was assessed using a one-dimensional internal ballistics simulation that assumes steady-state flow and neglects vertical-axis external forces. The objective was to determine the optimal trade-off between thrust management, propellant weight, and system simplicity.

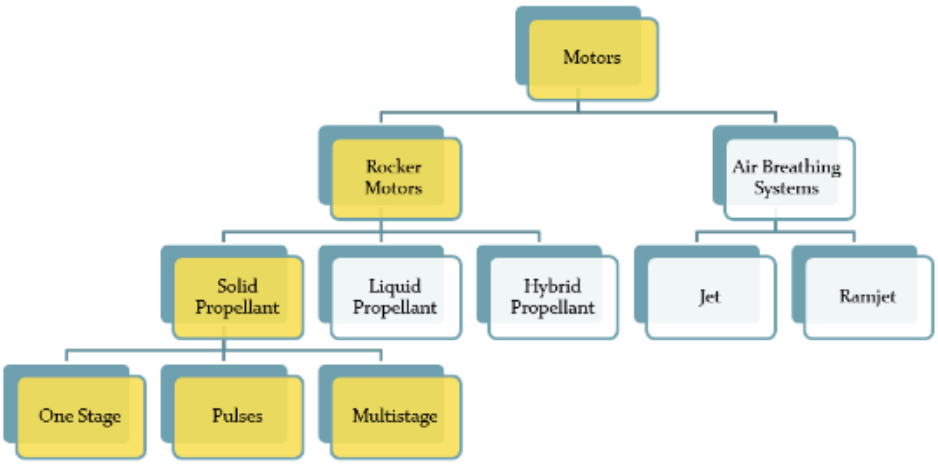

Figure 11. Missile propulsion motors alternatives.

4.1. Comparative analysis and simulation results

Numerical simulations of internal motor performance—including grain regression, thrust evolution, and propellant mass flow—are presented in **Figure 12**. The results were benchmarked using both total propellant mass and achievable mission profiles. Configuration-specific advantages and disadvantages are summarized in **Tables 2** and **3**. Based on this assessment, the most effective solution is a two-stage solid rocket motor featuring a dual-pulse second stage, confirmed by prior works in the literature [34,35].

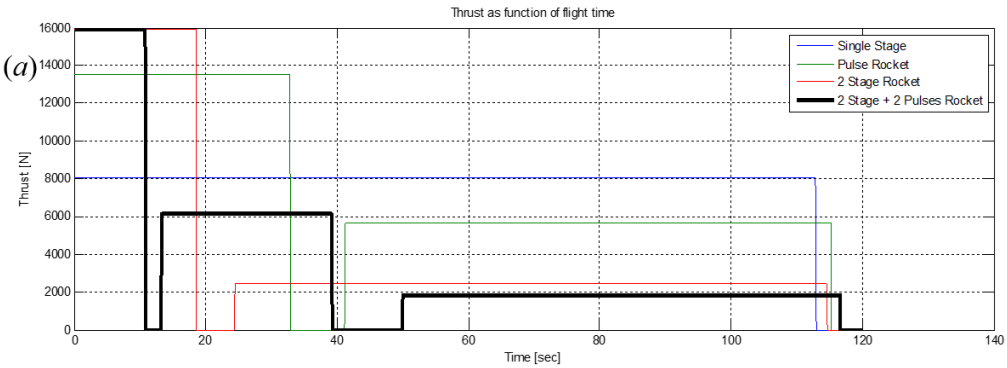

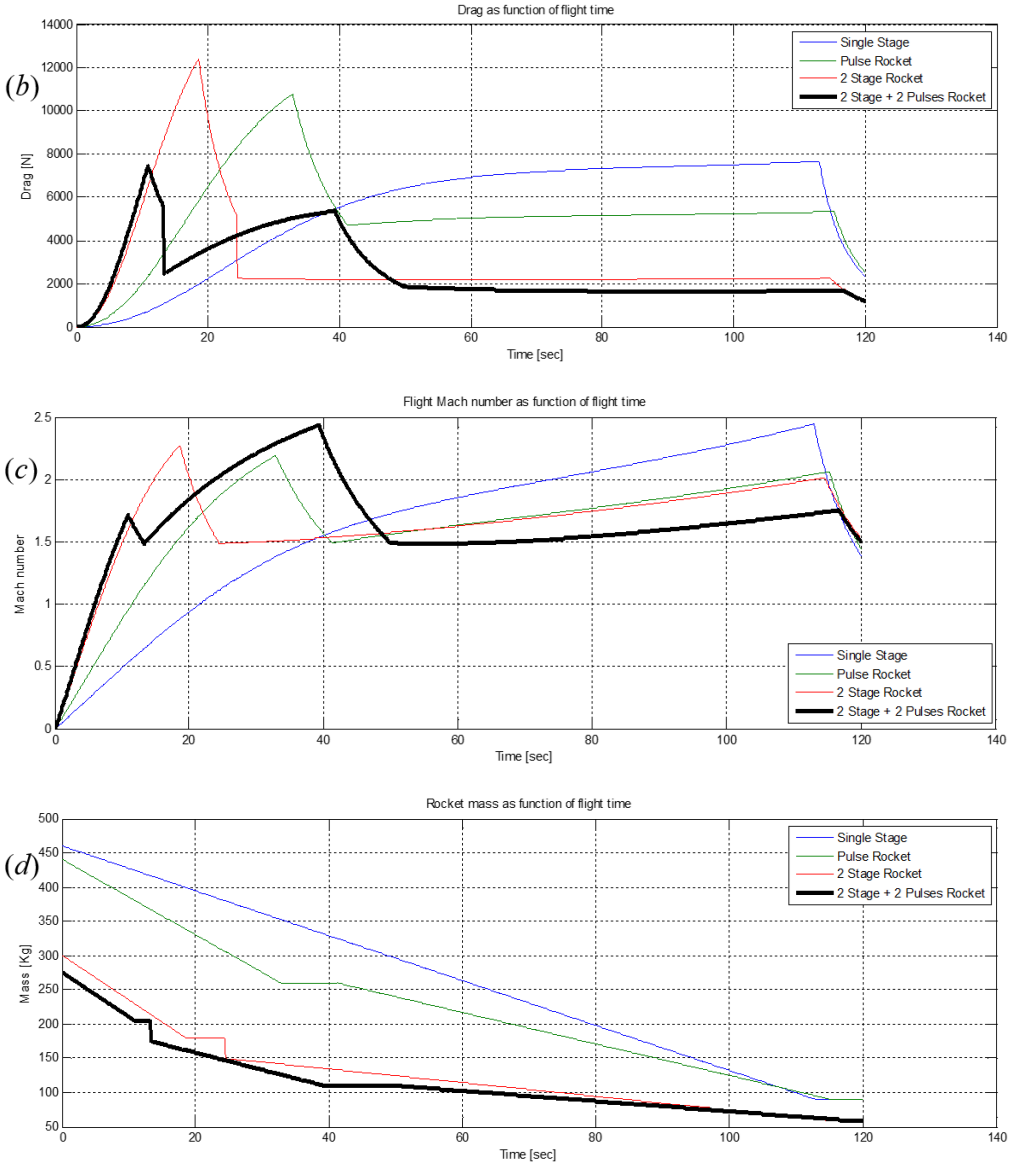

Figure 12. Comparison between different propulsion motors (single stage, pulse rocket, 2 stage rocket, 2 stage + 2 pulses rocket) drag force parameters versus time: **(a)** Thrust; **(b)** Drag; **(c)** Mach number; **(d)** Mass distribution.

Table 2. PDR propulsion motors configurations comparison for main parameters.

Criteria/Motor	Solid propellant	Liquid propellant	Hybrid	Ramjet—solid propellant	Turbo-jet
ISP [sec]	200–250	250–400	240–350	750	2000+
Thrust control—real time	Non-exist	Exist	Exist	Non-exist	Exist
Mechanical complexity (1—most simple, 5—most complex)	1	4	3	2	5
Flight velocity	No limit	No limit	No limit	Mach range: 2–6	Max. Mach 2
Cost	1	4	3	2	5
Additional limitations	Low safety	Expansive motor and complex structure		Dependent on external environment Initial acceleration is required Technological immaturity Suitable for high speeds only	Many moving parts and structure complexity Requires a very large diameter
More benefits	Cheap to produce				Ability to receive energy with the turbine assist

Table 3. PDR propulsion motors mass and diameter configurations comparison.

Parameter/motor type	One stage	Pulses	Two stages	Two stages missile with second stage based on two-pulses.
Diameters [mm]	300	300	300	300
			200	200
Propellant mass distribution [kg]	370	180	120	70
		160	90	65
				50
Total propellant mass [kg]	370	340	210	185
Weight saving percentage [%]	0	8.1	43.2	50
	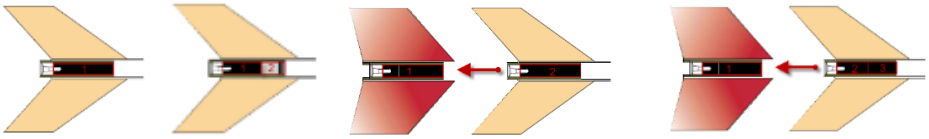			

This configuration was selected for its ability to deliver: (i) Rapid initial acceleration via a high-thrust booster stage. (ii) Controlled thrust sustainment through pulse separation in the second stage. (iii) Improved fuel efficiency and overall range-to-mass ratio. The selected propulsion design is illustrated schematically in **Figure 13**, with supporting data in **Table 4**.

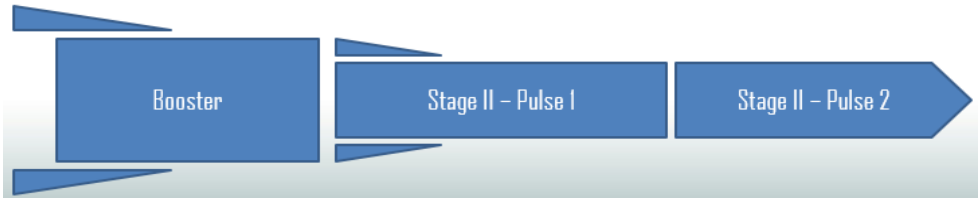

Figure 13. Selected propulsion system schematic configuration: Two-stages motors with the second stage based on two pulses.

Table 4. CDR selected propulsion system detailing.

Propellant property/Engine section	Booster	Pulse 1	Pulse 2	Total
Propellant mass* [kg]	80	70	75	225
External Diameter [mm]	300	200	200	
Mass flow [kg/sec]	10	2.05	1.15	
Propellant Burning rate [mm/sec]	8.8	40.6	22.8	
Chamber pressure [atm]	60	60	30	

Note: * Additional 7 percent propellant added to overcome losses.

4.2. Propellant composition and characteristics

Based on the materials study, the baseline propellant mixture consists of: (i) Binder: 14% Hydroxyl-Terminated Polybutadiene (HTPB). (ii) Oxidizer: 66% Ammonium Perchlorate (AP). (iii) Metallic additive: 20% aluminum powder (for energy density enhancement). (iv) Burning accelerant: Ferrocene or ferric oxide (Fe_2O_3). (v) Theoretical burning rate: 6.35–76.2 mm/sec (dependent on pressure

geometry). (vi) Grain geometry: Optimized star-grain configuration for high initial surface area and controlled burn back.

This formulation is selected for its balance between energetic density, thermal stability, and manufacturability.

4.3. Structural booster design and insulation

The SRM casing and thermal protection are designed to sustain high-pressure and high-temperature combustion. Key specifications include: (i) Motor Case: 5 mm thick heat-treated alloy steel. (ii) Thermal Insulation: Dual 5 mm layers of EPDM rubber reinforced with Kevlar fibers. (iii) Liner: Composite of HTPB and silica particles for chemical and thermal resistance.

4.4. Performance modeling and equations

In this early-stage analysis, the missile's axial velocity change (Δu) was estimated using a simplified one-dimensional equation that considers ideal exhaust velocity, drag, and gravity but omits vertical motion and lateral aerodynamic forces. The governing expression is:

$$\Delta u = -U_{eq} \cdot \ln\left(\frac{m}{m_0}\right) - \frac{\overline{D}}{m} \cdot \Delta t - gsin(\phi) \cdot \Delta t \tag{8}$$

where $\Delta u, U_{eq}, m_0, m, \overline{D}, g, \phi, \Delta t$ represent change in missile velocity over the time increment Δt [m/s], equivalent exhaust velocity (approximated as ideal) [m/s], initial total mass of the missile [kg], instantaneous mass [kg], average aerodynamic drag [N], gravitational acceleration [9.81 m/s^2], flight path angle [rad] and time step [s], respectively. This equation consists of three terms: (i) the Tsiolkovsky rocket equation, describing velocity gain due to fuel consumption; (ii) velocity losses due to drag; and (iii) gravitational deceleration quantification along an inclined flight path.

This formulation was used to compare the velocity efficiency of the propulsion configurations outlined in Sec. 4.1. The thrust and gas exit velocity (e.g., C-star (C^*) is a performance parameter for rocket engine propellants, representing the theoretical exhaust velocity achievable under ideal combustion conditions within the combustion chamber) have been calculated by the following equations alongside burning propellant parameters that appear in **Table 5**:

Table 5. CDR propulsion system parameters at 30 atm and 60 atm.

	Chamber pressure of 60 [atm]	**Chamber pressure of 30 [atm]**
I_{SP}	263 [sec]	262 [sec]
T_C	3447 [k]	3386 [k]
C^*	1583 [m/sec]	1577 [m/sec]
ρ_C	1768 [kg/m^3]	
γ	1.19	
M_W	26.2	

$$U_e = \sqrt{\frac{2\gamma \cdot R_0 \cdot T_C}{(\gamma - 1) \cdot M_w}\left[1 - \left(\frac{P_e}{P_c}\right)^{\frac{\gamma-1}{\gamma}}\right]} \tag{9}$$

where $\gamma, R_0, T_c, M_w, P_c, P_e$ represent specific heat ratio, universal gas constant, combustion chamber temperature, molecular weight of exhaust gases, and chamber and exit pressures, respectively.

The total thrust developed by the SRM is given by:

$$F = \dot{m} \cdot U_e \cdot \lambda_{nozzle} + (P_e - P_a)A_e \tag{10}$$

where $\dot{m}$, λ_{nozzle}, P_a, and A_c represent propellant mass flow rate, nozzle efficiency factor, ambient pressure, and nozzle exit area, respectively. For ideal expansion and negligible overpressure, Equation (10) simplifies to:

$$T = \dot{m}U_e + (P_e - P_0)A_e \tag{11}$$

where P_0 is the ambient pressure. Accordingly, the specific impulse, a key measure of propulsion efficiency, is determined by:

$$I_{sp} = T/\dot{m}g \tag{12}$$

The grain burn rate equation is:

$$\dot{r}_b = aP^n \tag{13}$$

where $\dot{r}_b$, a, n, and P are the linear burn rate [mm/s], the empirical coefficients: Pre-exponential coefficient (depends on formulation) and pressure exponent (typically between 0.3 and 0.6), and the chamber pressure, respectively. This formulation, combined with the star grain geometry, enables tailored thrust profiles and efficient burning combustion surface evolution over time (**Figure 14**).

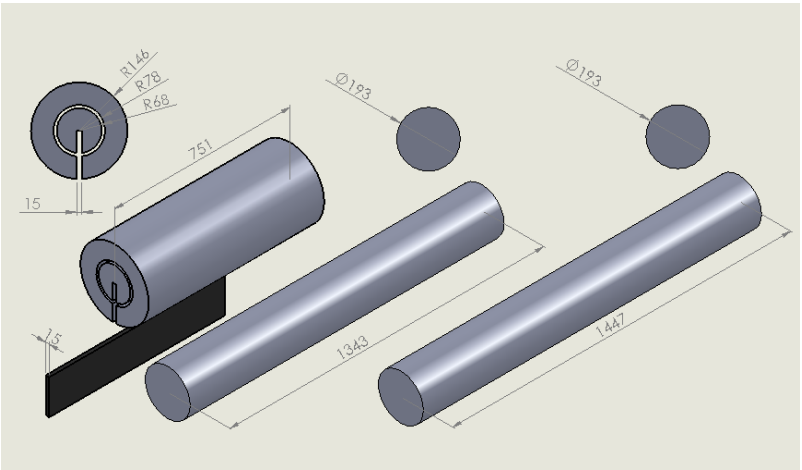

Figure 14. Grain geometry of booster and pulses' stage.

In summary, the two-stage solid rocket motor with a dual-pulse sustainer stage offers a robust balance of high thrust, controllable burn profiles, and optimized propellant mass. It fulfills mission constraints on acceleration, altitude, and range while remaining structurally compact and manufacturable within current solid-propellant technology frameworks.

5. Thermal barrier membrane and ignition system

5.1. The thermal barrier membrane

The thermal barrier membrane serves as a critical component in the dual-pulse solid rocket motor, enabling sequential combustion while thermally isolating the two chambers until activation of the second pulse. Its key design attributes are as follows: (i) Material: Flexible Ethylene Propylene Diene Monomer (EPDM) polymer. (ii) Geometry: Circular membrane with a diameter of 195 mm and thickness of 10 mm. (iii) Operational principle: As shown in **Figure 15**, the membrane is asymmetrically treated. One face is coated with a high-temperature-resistant material capable of withstanding the thermal flux generated during the first pulse combustion. The opposite face remains untreated. Upon ignition of the second pulse, elevated chamber temperatures exceed the thermal degradation threshold of the uncoated side, causing the membrane to melt or rupture, thereby allowing hot gases to flow into the secondary chamber without mechanical obstruction. This controlled failure mechanism ensures precise temporal separation between combustion events, contributing to optimized thrust management and motor stability.

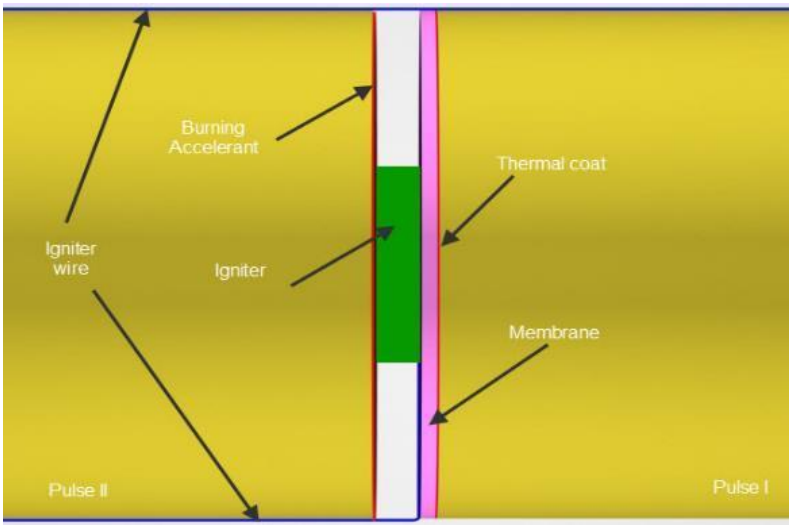

Figure 15. Thermal barrier schematic configuration.

5.2. The ignition system

The ignition system comprises high-reliability initiators precisely located to ensure consistent and sequential activation of each combustion chamber. Based on the schematics shown in **Figure 16**, the primary design features are as follows: (i) Igniter Type (**Figure 16a**): Exploding Bridge Wire (EBW) electrical initiator, a widely adopted solution in military-grade propulsion systems. (ii) Construction (**Figure 16b**): The igniter consists of a fine bridge wire, typically ranging from 0.02 mm to 0.10 mm in diameter, fabricated from low-resistance, high-conductivity metals. (iii) Materials: Platinum or gold are commonly used due to their predictable electrical and thermal properties. (iv) Activation Mechanism: A high-voltage pulse is applied across the bridge wire, vaporizing it almost instantaneously through resistive heating. This rapid phase change initiates a primary charge that ignites the solid propellant grain. (v) The

design and operational principles of the EBW initiators are well documented in the literature [36–39], providing both theoretical background and empirical validation. This ignition architecture ensures rapid, reliable motor start-up with minimal energy loss and excellent timing precision, both essential for the phased operation of a dual-pulse propulsion system.

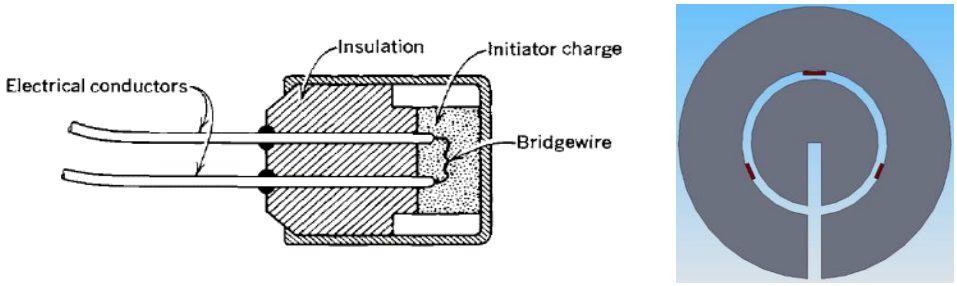

Figure 16. Igniter system: **(a)** Igniter schematic configuration and **(b)** Igniter location inside the propellant grain.

6. Structure

The structural design of the Horned-Viper missile is driven by mission-critical requirements and performance constraints established during the Preliminary Design Review (PDR) shown in **Figure 17** (especially in the aerodynamic sense). Key objectives for the structural configuration include: (1) Achieving a clean aerodynamic shape to minimize drag; (2) Accommodating internal volume for fuel, avionics, and the warhead; (3) Withstanding aerodynamic, inertial, and environmental loads; (4) Supporting the combined mass of propulsion and guidance systems; (5) Ensuring resistance to adverse weather conditions. (6) Providing a viable service life (shelf life and operational durability); and (7) Integrating with the launch platform architecture.

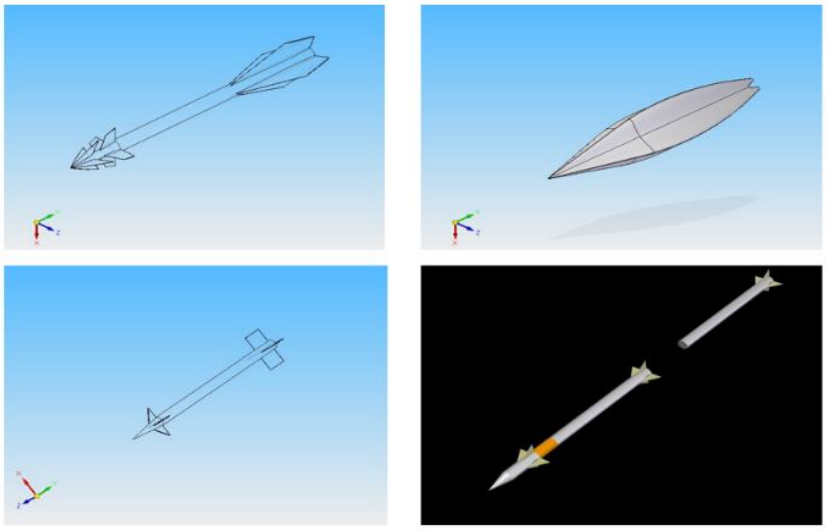

Figure 17. PDR missile structure concept.

As schematically illustrated in **Figure 18**, the overarching goal is to design the lightest possible structure capable of fulfilling all mission requirements. The structural

design process follows a stepwise methodology: (a) Definition of design criteria; (b) Selection of an appropriate structural concept; (c) Assessment of loading conditions (guidance and environmental loads); (d) Strength and aero-elastic analysis, including collapse and fatigue evaluation; (e) Final optimization.

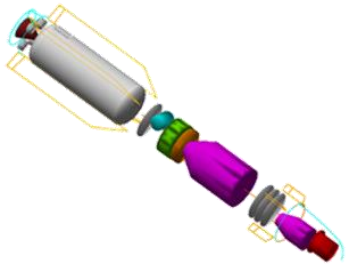

Figure 18. Structural schematic view.

Structural constraints include: (a) missile diameter: 0.2 m; (b) missile length: 3–4 m; (c) structural weight ≤ 90 kg; and (d) warhead weight = 20 kg. A comparative survey of candidate structural materials is provided in **Table 6**.

Table 6. Brief structural materials review.

Material/Parameter	Weight	Strength	Life cycle	Thermal durability	Casting and welding ability	Cost
Aluminum 2219/2024	Average	High	Low	Low	None	Average
Maraging Steel	Low	Very High	High	High	Weld-able	High
PH-15 Steel	Very low	Above average	High	Average	Weld-able	Low
Ti-6Al-4v	Average	Above average	High	Above average	Medium	Very high
Composite Graphite/Epoxy	High	High	Average	High	None	Very high

General structure configuration and material allocation will be elaborated. To meet mass, strength, and thermal resistance requirements, the missile structure is segmented into specialized components using optimized materials: (i) The propulsion assembly is divided into two discrete stages (see **Table 7**); (ii) The engine casings are fabricated from maraging steel, ideal for high-pressure, high-temperature combustion chambers; (iii) Aerodynamic control surfaces (fins and canards) are constructed from aerospace-grade aluminum alloys to reduce weight while maintaining sufficient strength; (iv) The missile nose cone (dome), exposed to peak thermal loads due to atmospheric friction, is manufactured from advanced ceramic composites to ensure structural integrity and thermal shielding. The PDR launch system structural concept is illustrated in **Figure 19**.

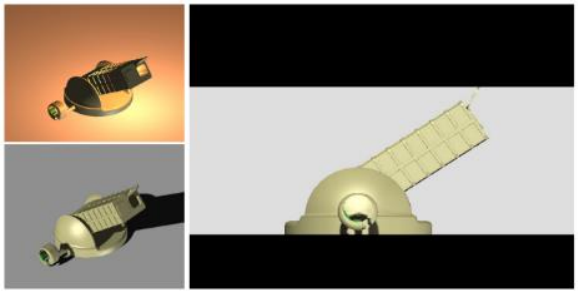

Figure 19. PDR launch concept.

Table 7. Missile components assembly table.

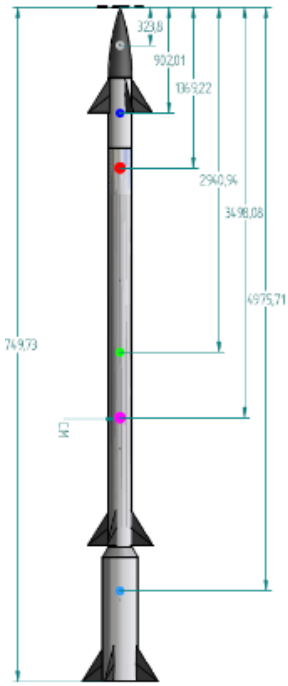

Component/Property	Weight (kg)	Length (mm)	Diameter (mm)	C.M (mm)	Iyy (kg·m²)	Ixx, Izz (kg·m²)
Dome	1.04	600	200	368.4	0.004	0.01
G&C	15.7	600	200	900	0.08	0.51
Warhead	21	350	198	1369	0.14	0.3
Motor	19.3	3367	200	3498	0.19	24.7
Propellant Pulse 1	70	1447	193	3763	0.32	10.6
Propellant Pulse 2	75	1343	193	2325	0.35	13.2
Booster	22.4	1088	300	4975	0.44	4.6
Booster Propellant	80	727	292	5050	2.64	0.67
Canards	5	300	200 (height)	-	-	-
Total Structure	95.7	5749	-	2787	1.01	300
Total Missile	333	5749	-	3500	2.7	700

The primary milestone objectives of the Critical Design Review (CDR) phase include: (i) Finalization of the missile's complete configuration (**Figure 20**); (ii) Compilation of a component specification table (**Table 7**) listing part dimensions, weights, centers of mass, and moments of inertia; (iii) Development of casing materials assignment (Dome: Silicon-Nitride, 3180 kg/m^3; G&C, Canards: Cover Material—Aluminum 2024, 2707 kg/m^3; Motor, Booster: Maraging Steel, 7479 kg/m^3; Target weight: 20 kg with density of 7479 kg/m^3) (iv) The final launcher design and deployment concept are depicted in **Figure 21**, aligning with both tactical mobility requirements and interface geometry constraints for the Horned-Viper missile system.

Figure 20. Final CDR missile configuration.

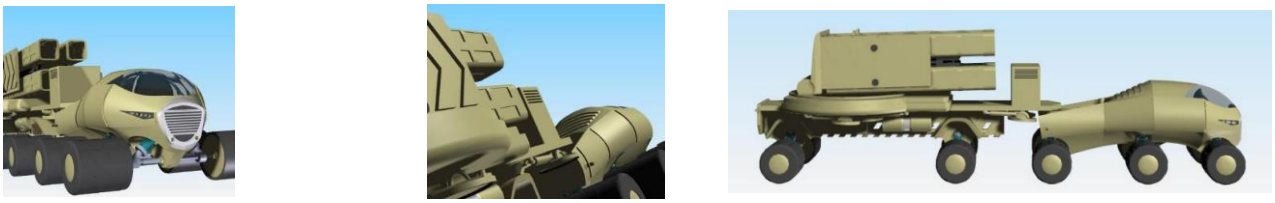

(a) **(b)** **(c)**

Figure 21. Launcher final schematic concept: **(a)** Front view of the launcher vehicle showing cabin and missile canisters; **(b)** Rear-side view highlighting the launcher mechanism and missile alignment; **(c)** Side profile of the complete launcher system with truck and trailer configuration.

6.1. Nozzle design: Geometry, materials, and equations

In accordance with design methodologies referenced in [25] and [40], the nozzle architecture adheres to the following principles: (i) Inlet angle: 40°; (ii) Exit angles: 25° and 13°, corresponding to the final two-thirds and first one-third of the nozzle length, respectively; (iii) Area ratio: The nozzle area expansion ratio is fixed at $\frac{A_e}{A_t} = 8.1$ to match sea-level exit pressure.

The nozzle throat area (A_t) is computed using the relation:

$$A_t = \frac{\dot{m}C^*}{P_c} \tag{14}$$

where $\dot{m}$, C^*, and P_c are propellant mass flow rate, characteristic velocity, and combustion chamber pressure, respectively. The nozzle efficiency (λ) (which is dependent on the deflection angle α_d) is used to estimate total thrust and is calculated according to the following relation:

$$\lambda = \frac{1+\cos(\alpha_d)}{2} \tag{15}$$

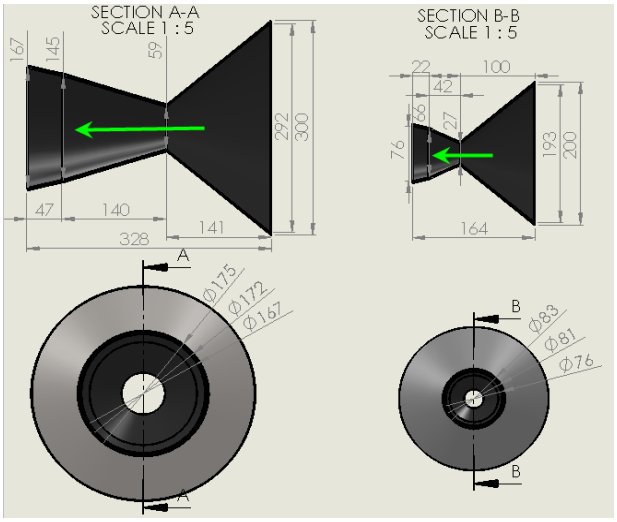

Figure 22. Nozzle structural design.

Table 8. Two-stages (booster + 2 pulses) nozzle geometry parameters.

Parameter/stage	Booster	1st + 2nd pulse
Entrance Diameter [mm]	292	193
Throat Diameter [mm]	59	27/28.2
Exit Diameter [mm]	167	76
Structure Thickness [mm]	1.5	1
Insulation [mm]	2.5	2.5
Exit Pressure [atm]	1	1, 0.5
Nozzle Efficiency	0.987	0.987

Nozzle materials include: (a) Structure: Heat-treated alloy steel; (b) Insulation: Dual-layer EPDM rubber and Kevlar fiber (calculated using the Nagler simplified

model [41] in Section 4 there); and (c) Throat insert: Pyrolytic graphite for thermal resilience. Geometry specifications for the dual-stage (booster + dual-pulse) nozzles are detailed in **Figure 22** and **Table 8**.

6.2. Pressure chamber design and stress analysis

Pressure chamber materials include: (i) Structure: Heat-treated alloy steel; (ii) Insulation: EPDM rubber and Kevlar fibers; and (iii) Liner: HTPB and silica compound.

Design parameters for the combustion chamber are tabulated in **Table 9** and shown in **Figure 23**. The design incorporates a safety factor of 2.0 to accommodate: surface imperfections, combined loading scenarios, thermal expansion and field handling wear.

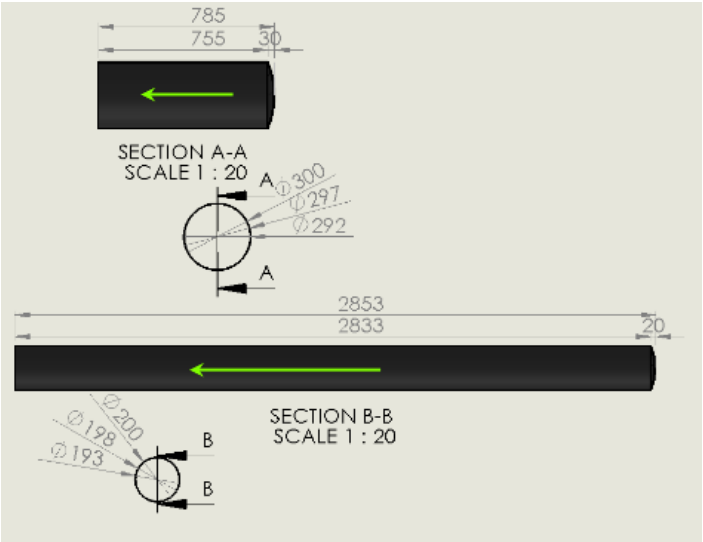

Figure 23. Cylinder chamber pressure geometry.

Table 9. Two-stages (Booster + 2 pulses) chamber geometry parameters.

Stage	Chamber Pressure [Pa]	Chamber radius [mm]	Tensile Strength [Pa]	Wall Thickness [mm]
Booster	6.07	150	1400	1.3
Pulse 1	6.07	100	1400	0.9
Pulse 2	3.035	100	1400	0.45

The hoop (circumferential) and longitudinal stresses developed in the chamber walls are given by:

$$\sigma_\theta = \frac{P_c r}{t}\,(\text{Hoop stress})\sigma_l = \frac{P_c r}{2t}\,(\text{longitudinal stress}) \tag{16}$$

Solving for wall thickness yields:

$$t = \frac{P_c r}{\sigma \cdot S.F.} \tag{17}$$

where $S.F.$ is the safety factor coefficient, r is the internal radius, and σ is the allowable material stress, respectively. The integrated assembly of the nozzle and pressure chamber is shown in **Figure 24**.

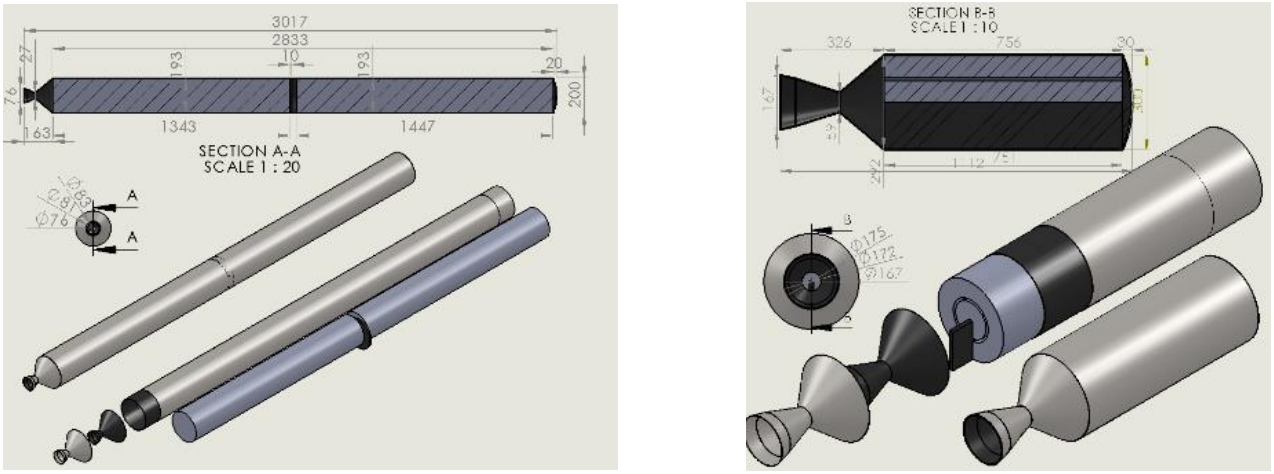

(a) **(b)**

Figure 24. Full two-stage: **(a)** Nozzle and cylindrical combustion chamber assembly and **(b)** Sub-assembly geometries.

7. Optimal rocket trajectory and thrust distribution

The missile trajectory equations of motion including the thrust force are:

$$\frac{dv}{dt} = \frac{T}{m} - g\sin\theta - \frac{D}{m} \tag{18}$$

$$\frac{d\theta}{dt} = -\frac{g}{v}\cos\theta + \frac{L}{mv} \tag{19}$$

$$\frac{dx}{dt} = v\cos\theta \tag{20}$$

$$\frac{dx}{dt} = v\sin\theta \tag{21}$$

$$\frac{dm}{dt} = -\frac{T}{gI_{sp}} \tag{22}$$

where the parameters $g, m, t, v, (x, y), A, C_d\ D, I_{sp}, L, T, \theta, \rho$ are the standard gravity acceleration [m/sec^2], projectile mass [kg], time [sec], projectile's velocity [m/sec], horizontal and vertical locations [m], projectile's reference area [m^2], drag force coefficient, drag force [N], specific impulse [sec], lift force [N], thrust [N], flight path angle [rad], and air density [kg/m^3], respectively.

The total delivered impulse T [Ns] formulation is:

$$T = \int_0^{t_{burn}} T(t)\mathrm{d}t \tag{23}$$

Based on Equations (18)–(23) and **Figure 25**, the following trajectory parameters were determined: Maximum altitude ($y_{\max}$) is achieved at t = 19.5 s while launch angles (θ) considered: 0° (horizontal launch) and 50° (lofted trajectory), with total delivered impulse: $T = 538.6\ \mathrm{kN \cdot sec}$. The total impulse of each stage separately

[kN · sec] was also calculated: (i) Booster: 190.7; (ii) Pulse 1: 171.3; (iii) Pulse 2: 176.6.

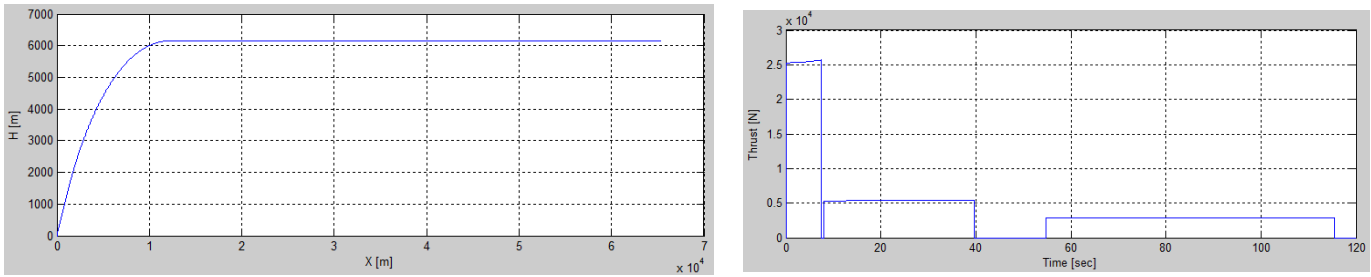

(a) **(b)**

Figure 25. Optimal rocket: **(a)** Trajectory and **(b)** Thrust distribution.

8. Servo actuation and control system

8.1. Servo architecture and mechanical interface

The general requirements for servo selection encompass key performance criteria across frequency, static, time-domain, and system-level considerations. From a frequency perspective, sufficient bandwidth is required to ensure dynamic responsiveness. Statics demand that the servo system provide maximum torque output aligned with the application's mechanical load. In terms of temporal behavior, the system must exhibit rapid rise time in response to step inputs, ensuring agility and precision. System-level factors include constraints on weight and volume, necessitating compact and efficient design. Accurate coupling mechanisms and high engine precision are essential for maintaining control fidelity. Additionally, the servo must effectively reject external disturbance torques while sustaining high reliability. Low power consumption is also a critical parameter, especially for applications with energy constraints or extended operational durations. This holistic view ensures that servo systems are selected and optimized for both mechanical performance and operational sustainability.

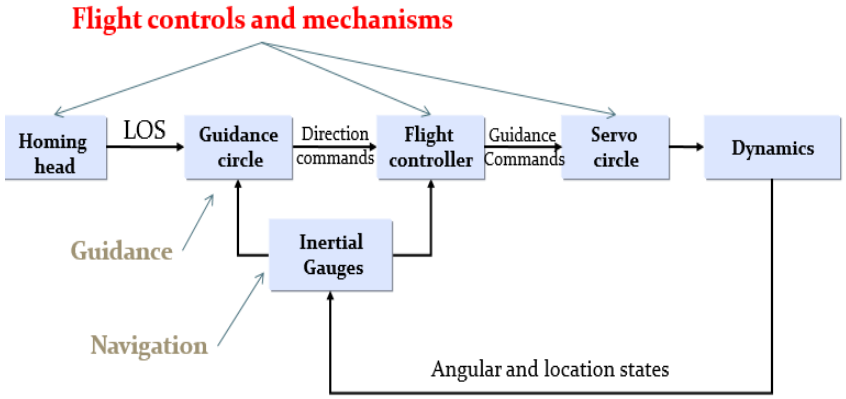

Figure 26. Flight control and mechanisms diagram.

Active angular stabilization is essential for modern interceptors to execute precise trajectory corrections and ensure high hit probability. The Horned-Viper's servo assembly governs canard and tail-fin deflections within the closed-loop guidance

framework depicted in **Figure 26**. The subsystem architecture comprises three sections with active angular stabilization (**Table 10**): (a) Steering: Actuator, transmission, and hinge that impart commanded deflections; (b) Flight Control: Linkages and bearings ensuring mechanical integrity under load; (c) Homing & Guidance: Inertial and seeker sensors generating error signals.

Table 10. Cons and pros of servo kind selection.

Servo kind	Benefits	Disadvantages	Remarks	types
DC	Interceptor missiles can also use an electric servo. Does not require an additional power supply Allows linear work	Does not require an additional power supply Allows linear work limited torque requires transmission	First-order system Relatively short time response	Brush, Brushless
Pneumatic	A pneumatic servo is suitable for missiles with strong maneuvers. Big torque per volume Requires less torque (“free steering”)	Heavy and complicated gas supply There are no continuous valves Non-linear, vibration-activated	Converts energy from pressure to mechanical work System dead time e^{-Ts}, $T \approx \frac{L}{a}$ Requires a compressed gas tank and/or compressor Controlled by a valve in a closed circuit	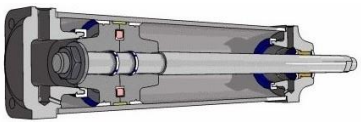 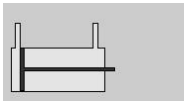

During PDR, candidate servomotors were ranked on torque density, volume, and mass (**Table 10**). By CDR, the selected unit combined surface, hinge, and transmission into a single assembly with total inertia J = 1.439 × 10^{-3} [kg·m^2] and worst-case maximum disturbance torque T_d = 35 N·m. A Crouzet geared motor type 801496–SNi10 (Max. peak torque 39 N·m, Nominal volt 24 V, Max. power 30 watts, 2.2 kg weight, 16 mm shaft hinge diameter, 188 mm servo motor length) was chosen (**Figure 27a**).

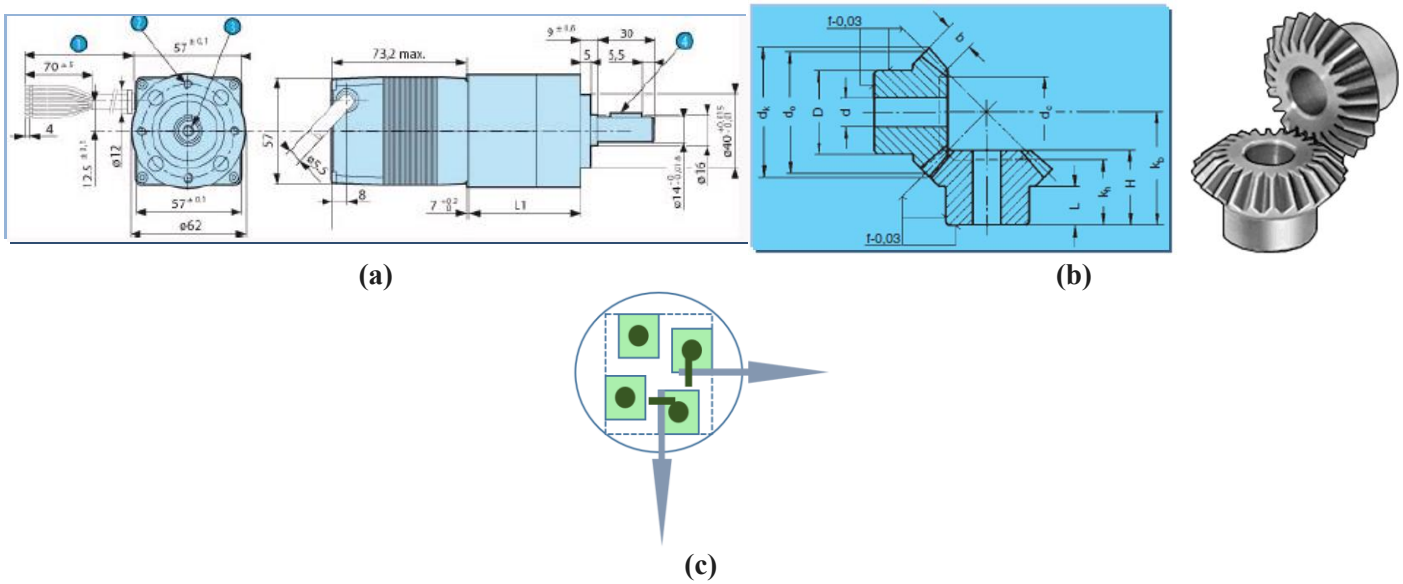

(a) **(b)**

(c)

Figure 27. Components and configuration of the actuator system: **(a)** Selected servo motor with dimensional specifications. **(b)** Selected bevel gear transmission with technical drawing and 3D view. **(c)** Assembly layout of the servo motor and transmission in the actuator system.

To transfer torque from the motor to the control surface at right angles, torque is relayed via a 1:1 miter gear ratio (Atlanta Drive Systems 1-40-25-126), rated to 55 N·m (max. hinge moment), 68.5 mm OD (outer diameter), 16 mm (H7) ID (internal diameter), and a weight of 0.93 kg, respectively (**Figure 27a**). Closed-loop target bandwidth was set to 10–30 Hz. Servo motor angular move is ± 20°. Details of servo assembly and transmission appear in **Table 11** and **Figure 27b,c**, respectively.

Table 11. Transmission versus motor parameters.

Transmission (X4)	Motor (X4)	Parameters
3.72 kg	8.8 kg	Weight
Pulse 2	120W	Power

8.2. PID controller design and tuning

A PID regulator (**Figure 28**) controls the missile canard deflection θ_C, with Laplace-domain law:

$$\theta_C(s) = K_P E(s) + K_I \frac{E(s)}{s} + K_D s E(s) \tag{24}$$

where $E(s)$ is the tracking error. The loop was shaped to a 10 Hz bandwidth ($2\pi \cdot \frac{10rad}{s}$ crossover $\geq 45^0$ phase margin) to ensure stability. K_P set proportional gain at crossover; K_I drove steady-state error to zero; K_D added phase lead for damping; and an anti-windup back-calculation prevented integrator saturation effects.

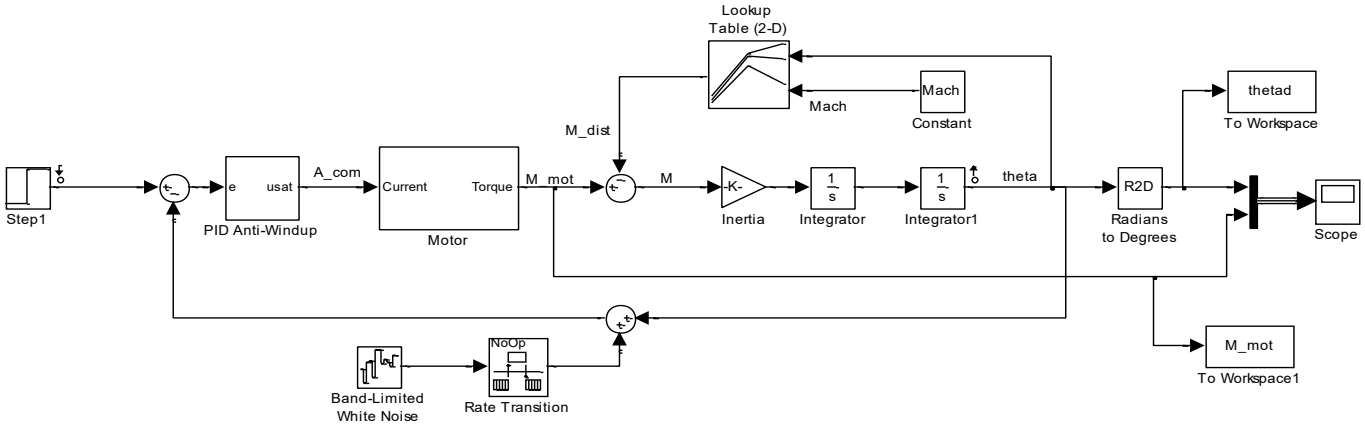

Figure 28. PID controller diagram.

8.3. Closed loop performance and simulation analysis

Nonlinear 6-DOF simulations with Mach-dependent loads and sensor noise yielded that Mach varying (20^o step): overshoot < 10% (**Figure 29**). Additionally, during nominal flight (20^o step), steady-state error < 0.5% (**Figure 30**). Finally, flight with noise, t_s increased by 10%, with anti-windup preserving precision (**Figure 31**). These results confirm the servo design and PID tuning meet the dynamic response requirements for high-speed intercept maneuvers.

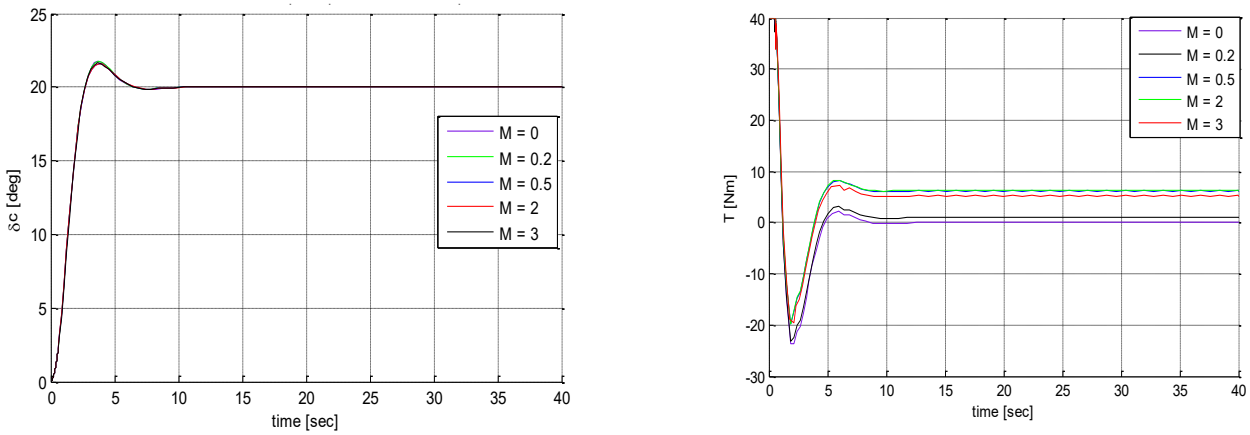

(a) **(b)**

Figure 29. Step response at 20° in closed loop for various typical *M* numbers: **(a)** Canard deflection; **(b)** Servo motor torque.

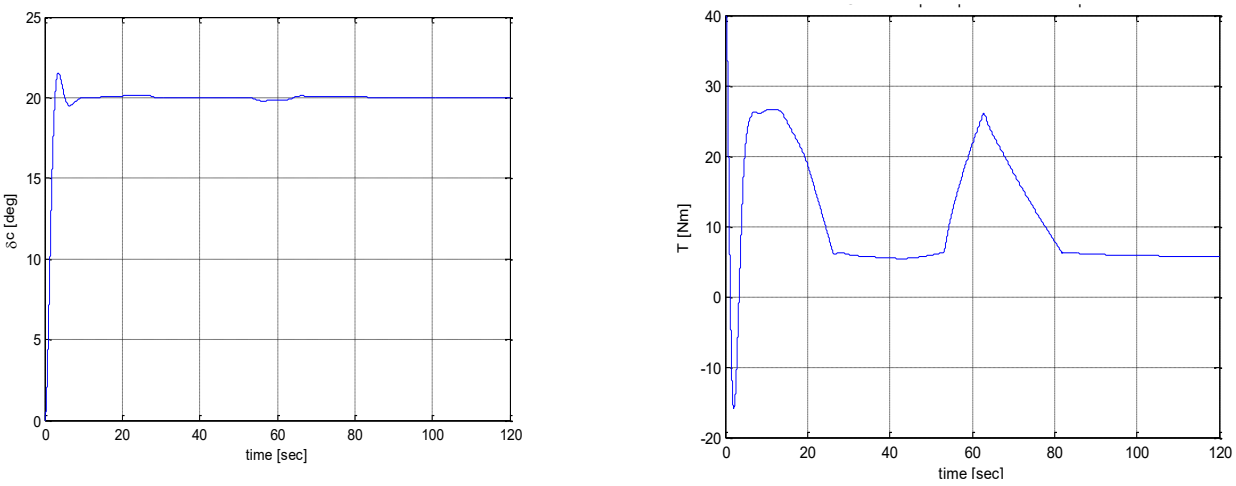

(a) **(b)**

Figure 30. Step response at 20° in closed loop at flight conditions: **(a)** Canard deflection; **(b)** Servo motor torque.

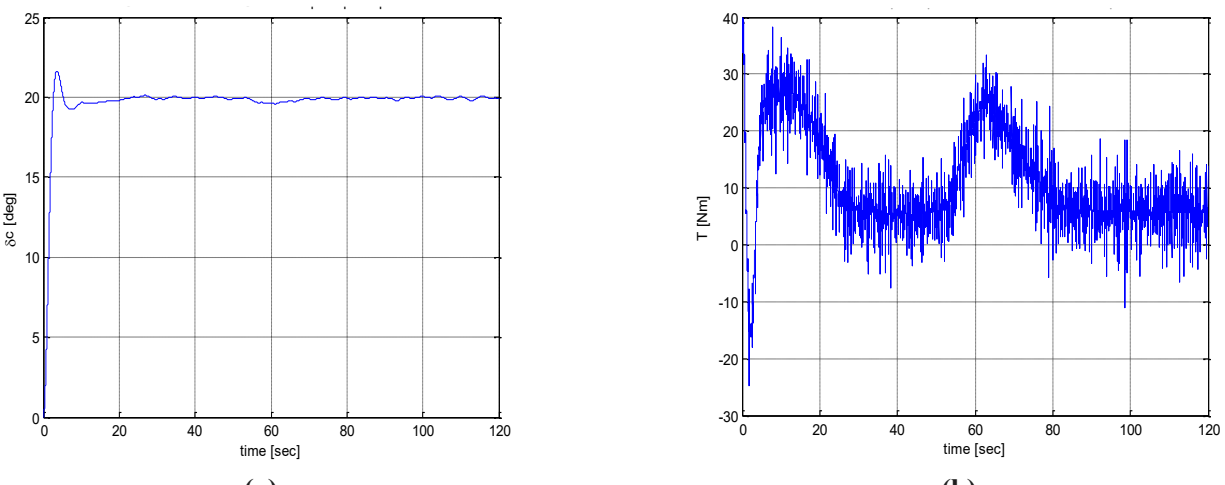

(a) **(b)**

Figure 31. Step response at 20° in closed loop at flight conditions with noise measurements: **(a)** Canard deflection; **(b)** Servo motor torque.

9. Guidance

The missile guidance system is defined schematically in **Figures 32** and **33**, respectively. e is the error of the missile's position relative to where it should be located according to a geometric rule, a_{M_c} is the lateral acceleration command of the missile, a_M is the lateral acceleration of the missile, a_T is the lateral acceleration of the target. The classical guidance methods (expansion) and their definitions, including advantages/disadvantages of each method are well elaborated in the Appendix alongside adequate illustrations. The missile guidance follows the PNG law $a_m = N(V_m \times \omega)$ where a_m, N, V_m, ω are the missile acceleration (**Figure 33**), the navigation constant (typically 3–5), missile velocity, and the line-of-sight rate, respectively.

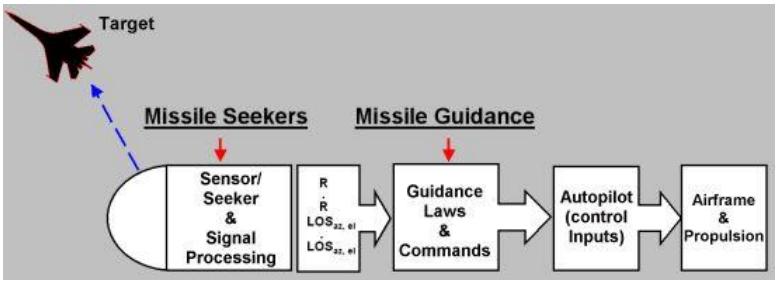

Figure 32. Guidance missile schematic view.

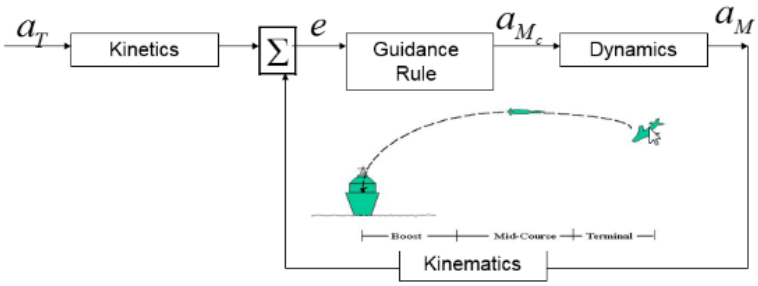

Figure 33. Guidance general closed loop rule.

10. Warhead

The warhead is the payload component of a missile, designed specifically to execute the destructive function for which the missile is launched. It constitutes the active element responsible for neutralizing or destroying the target, whereas the remaining missile components act as a delivery system. A warhead typically includes a destructive agent and, in many cases, a fragmentation enhancement known as controlled spray, intended to maximize lethality. This spray may consist of pre-formed fragments such as metal balls, cubes, steel shards, or improvised items (e.g., nails, screws). Common configurations involve concentric fragment rings around a cylindrical explosive core. The missile serves to deliver the warhead to the vicinity of the target. The primary goal of the warhead is to disable the target to a degree that it can no longer fulfill its intended function.

Types of Warheads: Hollow Charge: Contains a shaped explosive capable of penetrating armor, typical in anti-tank munitions; Tandem Charge: Comprises two consecutive hollow charges; the first defeats reactive armor, and the second penetrates

the main armor; Conventional: Employs standard explosive material; Illuminating (Lighting): Emits light to illuminate large areas; used in artillery and mortars; SABOT (Armor-Piercing Fin-Stabilized Discarding Sabot): Features a high-density metal penetrator (e.g., tungsten or depleted uranium) accelerated to extreme velocities using kinetic energy. These rounds lack fuses and rely on momentum; Anti-Personnel (Flechette): Disperses thousands of miniature darts to target infantry; typically deployed from tanks.

Warhead construction (**Figures 34** and **35**) is made of (i) Explosive Types: Conventional: Fragmentation-based explosives; Unconventional: Includes chemical, biological, and nuclear payloads. (ii) Detonation Mechanisms: Contact Fuse: Triggers upon direct impact; Time Fuse: Detonates after a preset delay; Altitude Fuse: Activated at a specific altitude using barometric pressure sensors; Proximity Fuse: Initiates detonation at a predefined distance from the target using electro-optical or electromagnetic sensors.

Figure 34. Typical guided weapons component layout.

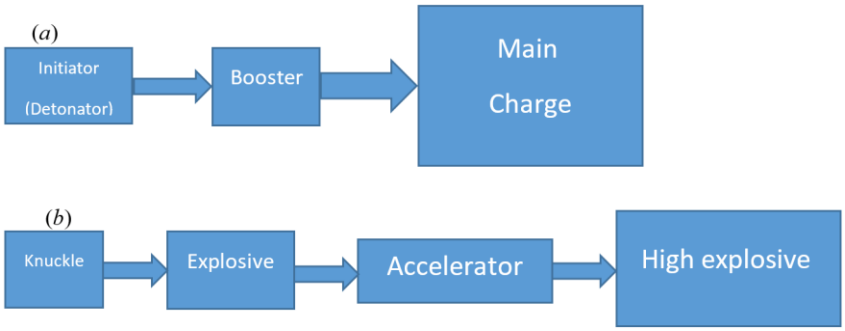

Figure 35. Explosive train: **(a)** Initiation chain; **(b)** Detonation chain.

Proximity fuses offer superior effectiveness but may add weight and cost. Stabilization improves warhead aerodynamic stability and accuracy. Methods include: (i) Spin stabilization: Achieved through rifled barrels. (ii) Fin stabilization: Common when the length-to-diameter ratio exceeds 5:2. Exceptions include shaped charges, which typically require fin stabilization regardless of dimensions.

Initiation and detonation chain (**Figure 35**): The detonation process progresses through a detonation train composed of: (1) Initiator/Detonator: Sensitive materials that begin the explosive sequence via impact or electric charge. (2) Booster/Accelerator: Amplifies and transmits the detonation to the main charge. (3) Main charge: Executes the primary explosive action. Explosive train reliability and safety are critically dependent on material sensitivity; overly sensitive materials risk accidental initiation.

Warhead effect and distribution: Fragmentation patterns (**Figure 36a**) typically follow a normal distribution. The effective damage radius (**Figure 36b**) is influenced by fragment shape and density. Spherical fragments are preferred for their low drag and optimized ballistic coefficients (**Figure 36c**).

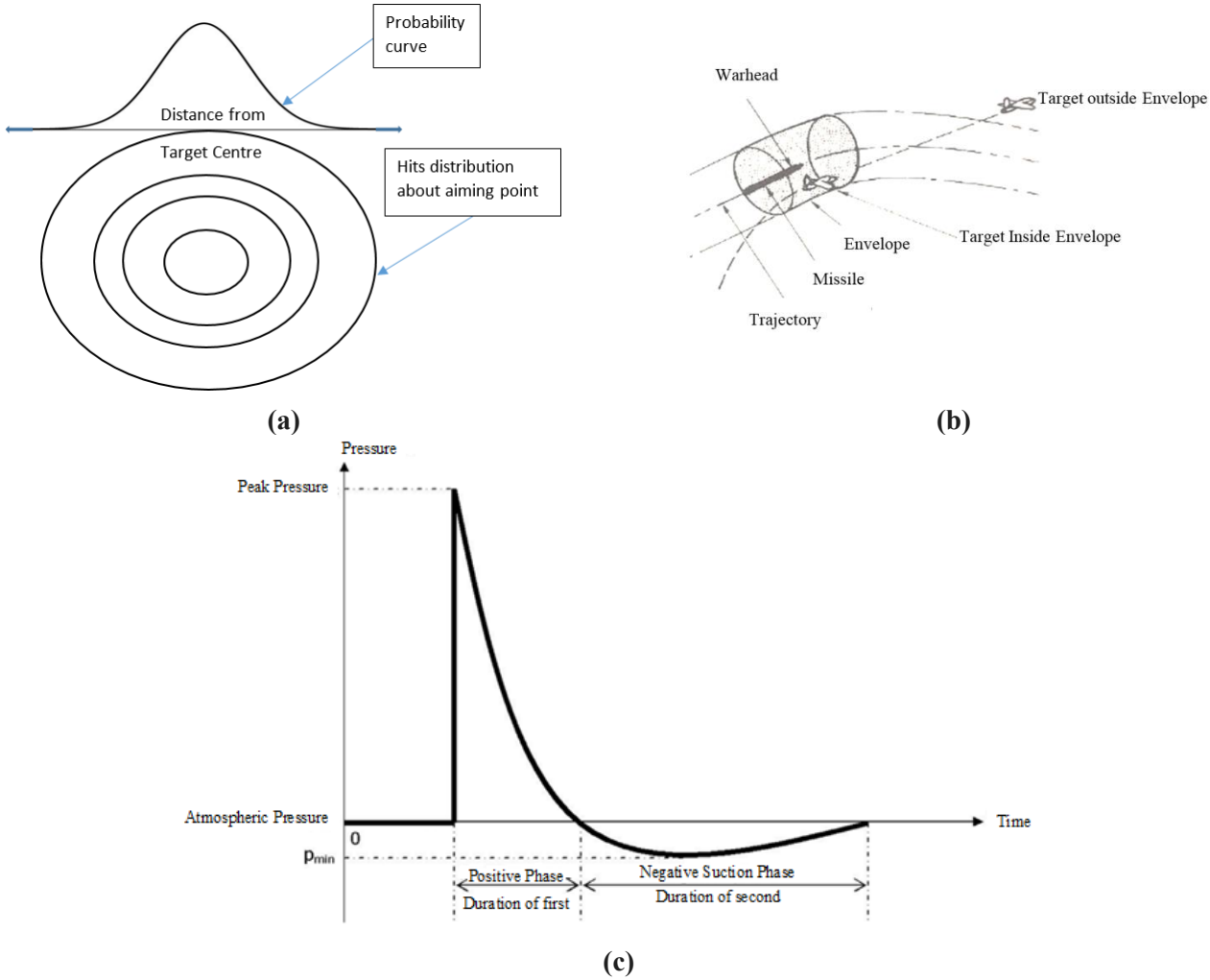

Figure 36. Warhead effect and distribution: **(a)** Hits normal dispersion; **(b)** Explosive envelope (damage volume); and **(c)** Pressure vs. time blast wave curve (Friedlander curve).

Finally, design recommendations are: (1) Maximize internal volume for explosive content. (2) Integrate concentric fragmentation layers for enhanced dispersion. (3) Employ spherical fragments to achieve wide-area lethality with lower mass. The final warhead geometry design include: (outside diameter: 168 mm, inside diameter: 120.5 mm, Long: 350 mm) with RDX-B explosive material and a total mass of 6 kg.

The ballistic shape coefficient quantifies aerodynamic efficiency:

$$\mathrm{C} = m_{frag}/C_D A \tag{25}$$

where the drag coefficient, cross-sectional area, and mass of the fragment are demoted by C_D, m_{frag}, A, respectively. Observation in Equation (25) learns that the density and shape of the body are critical and affect the quality/ballistic coefficient. In accordance with this, the common materials used in the warhead—fragmentation components—are tungsten, uranium and steel, which have a high density per volume. The preferred shape for low drag is spherical. In conclusion, it is obtained that for a fragmentation warhead, a larger dispersion cloud will be obtained (up to about 15 m) despite its low

mass because its spherical drag coefficient and low cross-sectional area compared to a rod warhead are an advantage for its selection.

Spherical fragmentation warhead calculations:

The general parameters are: warhead mass ($m_{waread} = 20$ kg); Mach range ($1.5 \leq M \leq 4$); missile diameter ($D = 0.2$ m); ratio of specific heats ($\gamma = 1.4$); ambient temperature at sea level ($\gamma = 1.4$); ambient temperature at sea level ($T_{sea-level} = 15\,℃ = 288$ K); air density ($\rho_{air} = 1.225\ \frac{\mathrm{kg}}{\mathrm{m}^3}$); $R_{specific,dry\text{-}air} = 287\ \frac{\mathrm{J}}{\mathrm{kgK}}$; miss distance = 10 m; the velocity range of the spherical fragments is derived using the equation:

$$V = M\sqrt{\gamma RT} \rightarrow 476.24 \leq V \leq 1360.7\ \frac{m}{s} \tag{26}$$

The initial fragment evaluation will be performed through Gurney equations and energy balance at the moment of missile shell explosion. Using energy balance at detonation, the following relation is used:

$$\frac{1}{2}\left(m_{frag} + c \cdot \varepsilon\right) \cdot V_0^2 + f m_{frag} = \eta \mathrm{ec} \tag{27}$$

Solving Equation (27) for V_0:

$$V_0 = \sqrt{2\frac{\eta \cdot \mathrm{e} - \mathrm{f} \cdot \frac{m}{\mathrm{c}}}{\frac{m}{\mathrm{c}} + \varepsilon}} \tag{28}$$

where m is the total fragmentation mass, c—the total explosive material mass, f—specific work to break the missile shell, e—specific explosive energy, and η—the explosive material efficiency ($\eta = 1$ for full efficiency). ε—The relative fraction of the explosive that accumulates kinetic energy ($\varepsilon = 0.5$ for cylinder shape). Assuming $\cdot\,\mathrm{e} \gg \mathrm{f} \cdot \frac{m}{\mathrm{c}}$, simplifies relation (28) to:

$$V_0 = \sqrt{2\mathrm{e}}\sqrt{\frac{1}{\frac{m}{\mathrm{c}} + 0.5}} \tag{29}$$

As the total mass of the fragments decreases in relation to the high explosive, then we will get a higher exit velocity, letting $\sqrt{2\mathrm{e}}$ be the Gurney energy of the explosive material. The selected energetic explosive will be RDX over HMX since it is much cheaper and has a similar Gurney energy value ($2930\ \frac{\mathrm{m}}{\mathrm{sec}} < 2970\ \frac{\mathrm{m}}{\mathrm{sec}}$), such as:

$$V_0 = 2930\sqrt{\frac{1}{\frac{m_{frag}}{\mathrm{c}} + 0.5}} \tag{30}$$

where $0 < \frac{\mathrm{m_{frag}}}{\mathrm{c}} < 1$. Equation (30) is exhibited in **Figure 37**, while $\frac{m_{frag}}{\mathrm{c}} = 0.7$ (balls total mass to total explosive material mass ratio) for fragmentations initial velocity of 2675 m/sec.

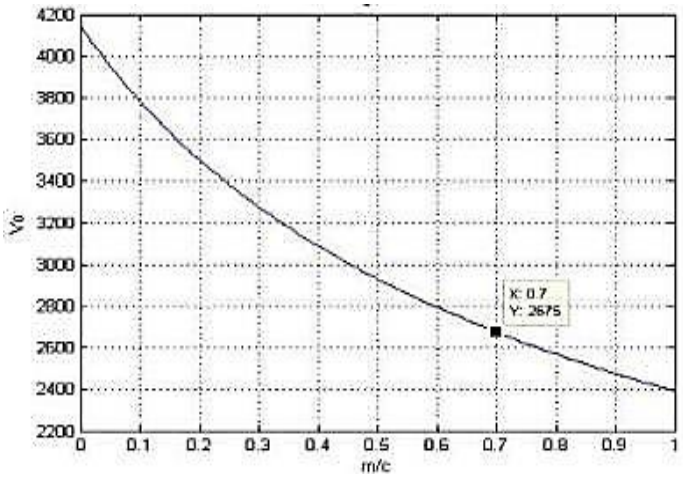

Figure 37. Fragmentation initial velocity versus balls' total mass to total explosive material mass ratio curve.

In the case of atmosphere-free flight, the only force acting on the fragmentation during its flight is the drag force presented by:

$$F_D = \frac{1}{2} C_w \rho_{air} A V^2 \tag{31}$$

Using the relation from Newton's 2nd law, $F_D = -ma = -m\frac{dV}{dt} = -m\frac{dV}{dx}\frac{dx}{dt} = -m\frac{dV}{dx}V$, and substituting it into Equation (31) yields:

$$-m\frac{dV}{dx}V = \frac{1}{2} C_w \rho_{air} A V^2 \tag{32}$$

Applying algebraic manipulation over (32) gives:

$$\frac{dV}{V} = -\frac{C_w \rho_{air} A}{2m} dx \tag{33}$$

With the following boundary conditions:

$$V|_{x=0} = V_0, V|_{x=x} = V \tag{34}$$

Which turns (33) into:

$$V = V_0 e^{-\frac{C_w \rho_{air} A}{2 m_{ball}} x} = V_0 e^{-0.75 C_w \frac{\rho_{air} x}{\rho_m d}} \tag{35}$$

where $A_{ball} = \pi \mathrm{d}^2/4$, $m_{ball} = \rho_m \pi \mathrm{d}^3/6$, d is the ball diameter, and A_{ball} is its section such that the ratio A_{ball}/m_{ball} equals $\frac{A_{ball}}{m_{ball}} = \frac{3}{2\rho_{\mathrm{m}}\mathrm{d}}$. The air density is $\rho_{air} = 1.225\ \mathrm{kg/m^3}$, the iron ball density is $\rho_m = 8000\ \mathrm{kg/m^3}$, and $C_w = 0.97$ (deformation caused by crashing through air shock wave). Now, substituting the initial velocity $V_0 = 2675\ \mathrm{m/sec}$ (30) into (35) alongside given parameters, Equation (35) becomes:

$$V = 2675 e^{-1.114 \cdot 10^{-4} \frac{x}{d}} \tag{36}$$

At $x = 10$ m Equation (36) becomes:

$$V = 2675e^{-\frac{1.114}{d}} \tag{37}$$

Plotting Equation (37), ball size is determined to be $d = 9$ mm, as shown in **Figure 38** at the beginning of the knee/bending curve profile. Accordingly, Equation (36) takes the form (M. K. S. units):

$$V = 2675e^{-12.377 \cdot 10^{-3}x} \tag{38}$$

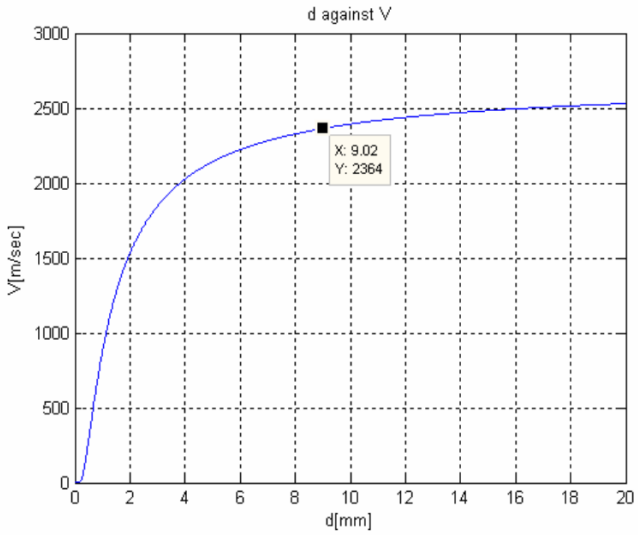

Figure 38. Fragmentation velocity versus ball diameter.

To establish the minimum number of spherical fragments required per cylindrical ring to guarantee a target hit at a distance of 10 meters, an average target cross-section diameter of 1.8 m (representative of a jet fighter) is assumed. The worst-case engagement occurs when the target moves perpendicularly to the fragment trajectory, exposing its minimal frontal area (**Figure 39a**). To ensure at least three fragment impacts under such conditions, the spatial distribution must account for an angular separation α between adjacent spheres (**Figure 39b**), spanning a full 360° ring. The number of spheres is then defined by the condition of maximizing angular coverage, with sphere diameter calculated as the ring circumference divided by the total number of spheres.

$$\sin\alpha = \frac{D_0/2}{R} = 0.09 \rightarrow \alpha = 5.16^0 \tag{39}$$

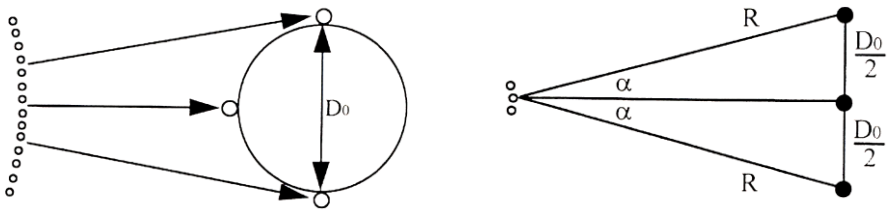

(a) **(b)**

Figure 39. Fragmentation locations versus target locations geometric analysis: **(a)** Schematic view; **(b)** Geometrical analysis for three fragmentations' spheres.

As an alternative approach, the calculations can be verified by solving the time-dependent equilibrium differential equation in X-Y-Z Cartesian coordinates within a cylindrical system:

$$m\ddot{x} = -\frac{1}{2}\rho S C_W (\dot{x})^2 \tag{40}$$

In this context, the displacement and its temporal derivatives are denoted by $\dot{x} = \frac{\partial}{\partial t}$, $\ddot{x} = \frac{\partial^2}{\partial t^2}$, respectively. The corresponding initial conditions are specified as $x(0) = 0, \dot{x}(0) = V$. These definitions enable the analytical determination of the number of spherical fragmentation elements distributed along a complete ring configuration as follows:

$$n_{min} = \frac{2\pi}{\alpha} = 70 \tag{41}$$

For a missile diameter of 0.2 m and 70 fragments per ring, the individual ball diameter is calculated as $d = \frac{\pi D}{n_{min}} = \frac{0.2\pi}{70} = 9$ mm. The linear trend (fire distance curve versus spatial angle) in **Figure 40** results from the short engagement distance. The total fragmentation mass per ring is then determined accordingly:

$$m_{frag} = \frac{n_{min}\rho_m \pi d^3}{6} = 70 \cdot 3.054 \cdot 10^{-3} = 0.214 \text{ kg} \tag{42}$$

where $m_{ball} = 3.054 \cdot 10^{-3}$. Given a mass of fragmentation $m_{frag} = 0.214$ kg, the corresponding explosive mass is determined using the established mass ratio (Equation (24), **Figure 40**).

$$\frac{m_{frag}}{\mathrm{c}} = 0.7 \rightarrow \mathrm{c} = 0.306 \text{ kg} \tag{43}$$

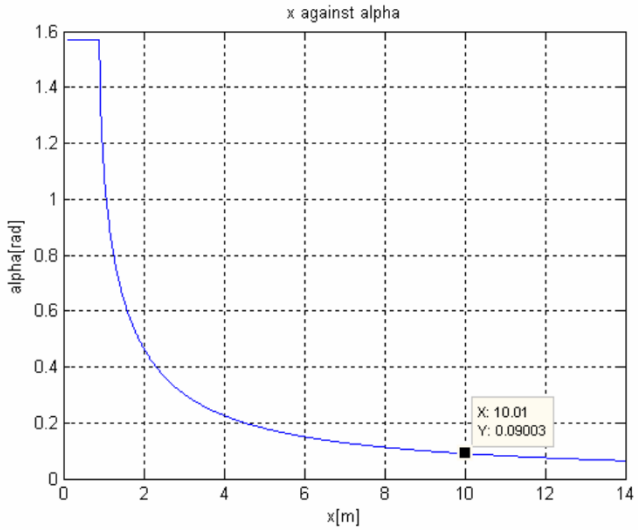

Figure 40. Simulation of fire distance versus spatial angle α between two adjacent fragmentations.

The warhead length is constrained by a total weight limit of 20 kg. Since the number of effective fragments scales with the number of rings, the maximum feasible

number of rings is computed by dividing the total allowable mass by the combined mass of a single fragment ring and its associated explosive charge according to:

$$N = \frac{m_{waread}}{m_{frag} + \mathrm{c}} = \frac{20}{0.214 + 0.306} = 39 \tag{44}$$

Accordingly, the warhead length will be:

$$L = Nd = 39 \cdot 0.009 = 0.35m \tag{45}$$

Of course, the spherical ball fragmentations total number will be:

$$N_{balls} = Nn_{min} = 39 \cdot 70 = 2730 \tag{46}$$

Refer to the schematic representation of the spherical fragmentation warhead in **Figure 41**. Subsequently, the analysis proceeds with evaluating the missile shell penetration and initiation phase of the high explosive, ensuring alignment with defined performance criteria.

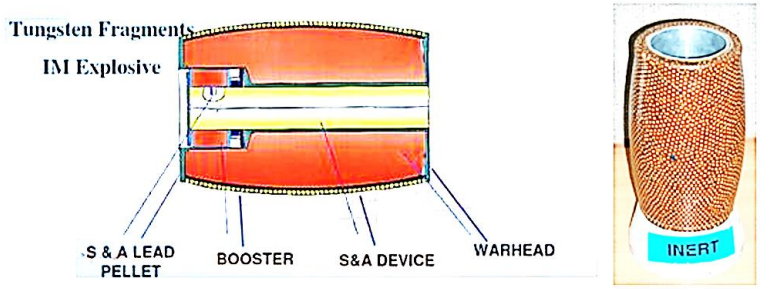

Figure 41. Example of a warhead based on spherical fragmentations.

Preliminary warhead design: In the conceptual design phase, the warhead architecture is based on a mechanical piston system, comprising a spring and bar mechanism enclosed within a cylindrical casing. This cylinder contains high explosive material and is encased by spherical metallic fragments, as illustrated in **Figure 42**. The force equilibrium between the spring and piston is governed by the following expression:

$$F = kx = P_0 A_{pump} = P_0 \frac{\pi D^2}{4} \tag{47}$$

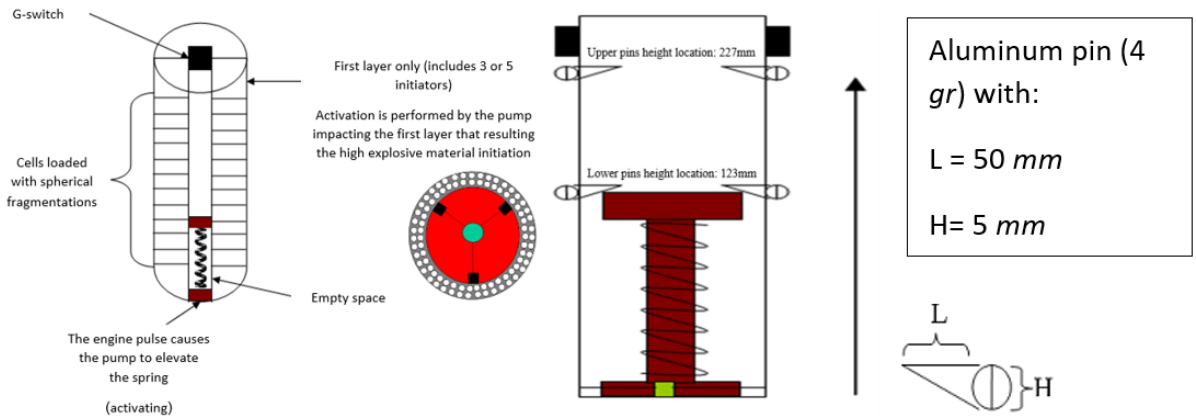

Figure 42. Preliminary design planning scheme of the warhead internal mechanical mechanism.

Here, the anticipated engine-generated pressure is denoted as $P_0 = 60$ atm, and A_{pump} represents the cross-sectional area of the piston oriented perpendicularly to the spring force. The parameters $k\ \left[\frac{N}{m}\right]$ and $x\ [m]$ correspond to the spring stiffness coefficient and the warhead's axial length, respectively. Based on these definitions, the required piston diameter can be derived using the following expression:

$$D = \sqrt{\frac{4kx}{P_0\pi}} = \sqrt{\frac{4 \cdot 11.37 \cdot 10^3 \cdot 0.33}{60 \cdot 101325 \cdot \pi}} = 28 \text{ mm} \tag{48}$$

It is feasible to select a desired direction in real time via a ground-based wireless control system, enabling the targeting of a specific region with a high probability of inflicting critical damage. However, incorporating such a control mechanism increases the overall system complexity and cost. It is important to note that the lethal radius of the fragments is estimated using the following relation:

$$R = \frac{1}{2}\frac{V^2}{g} \tag{49}$$

For 9 mm steel spherical fragments, the estimated lethal radius is approximately 15 m. Following the evaluation of three alternative fragmentation warhead concepts (as presented in the Appendix), the configuration based on spherical fragmentation distribution was selected. This decision was guided by the following primary considerations. A significantly higher probability of inflicting damage due to the large number of individual fragments; Reduced aerodynamic drag relative to alternative configurations; Enhanced ease of dispersion, enabling greater directional control; Lower production costs and ease of manufacturing.

The optimal initiation method for the warhead involves asymmetric initiation, as illustrated in **Figure 43** and detailed in the Appendix, which explores the distribution of directional fragmentation sprays. The use of 3 or 5 initiators (length = 127 mm, width = 21 mm, height =19 mm, weight = 75 gr, volume = 0.05 mm^3) yields higher percentages for both fragment hits and explosive energy utilization, attributed to the symmetric geometry of the cylindrical warhead. Consequently, based on cost-efficiency and weight constraints, the configuration incorporating three symmetrically arranged initiators was selected. Analytical modeling has indicated that the deployment of approximately 5953 spherical fragments is sufficient to neutralize the target.

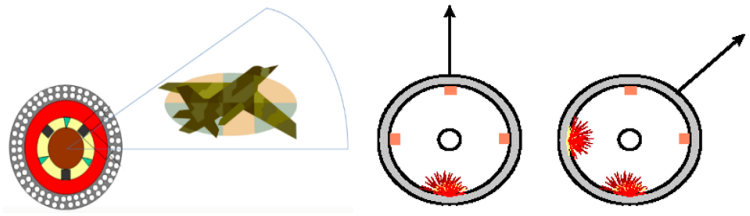

Figure 43. Asymmetrically initiated warhead operation scheme.

The directional warhead is characterized by its ability to inflict damage within a defined region at a specified range, thereby enabling increased fragment density in the target area. Its operational objective is to strike the target in any orientation that

compels mission termination. The preferred impact direction can be determined and commanded remotely from the ground. The functional concept of the directional warhead is depicted in **Figure 44**, while the mechanical implementation is outlined in **Figures 45** and **46**.

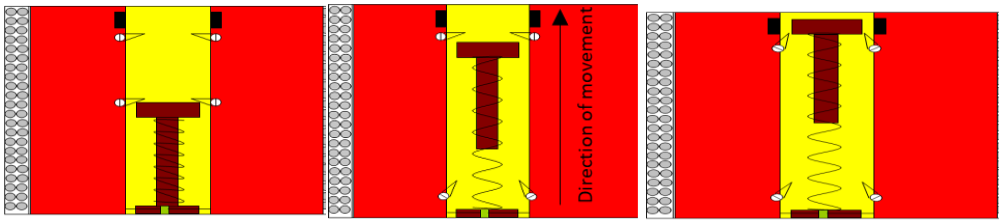

Figure 44. Three-steps warhead piston mechanism operation concept while tap switch (power source = thermal battery): **(a)** Step 1; **(b)** Step 2; **(c)** Step 3.

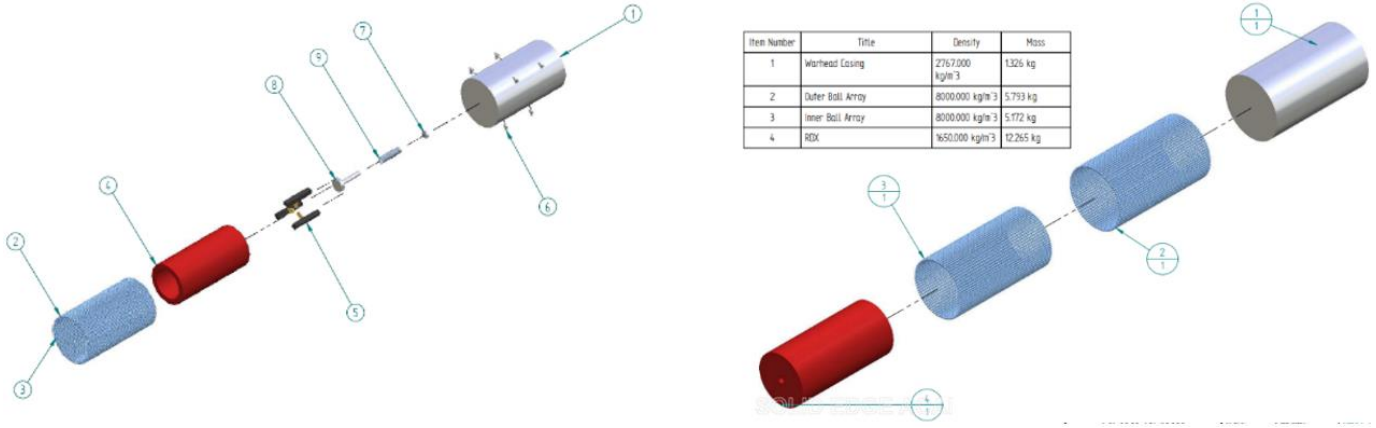

Figure 45. Warhead CDR assembly illustration.

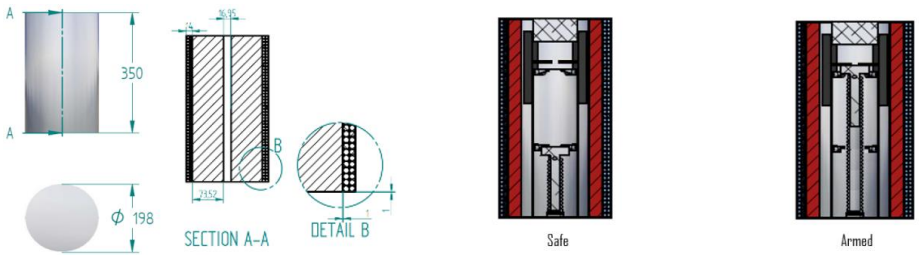

Figure 46. Warhead final schematic (CDR) mechanism: **(a)** Warhead detailed CDR concept; **(b)** Safety mechanism operation concept.

10.1. Design summary

The warhead is designed using RDX as the primary explosive material, selected for its favorable balance of cost and performance, which closely aligns with that of HMX. Fragmentation is achieved using spherical steel balls, chosen after comparative analysis of various concepts. This configuration enhances lethality by maximizing the number of uniformly distributed fragments while minimizing aerodynamic drag and manufacturing complexity. The directional efficiency of the warhead is further improved through this arrangement, enabling concentrated fragmentation within a

targeted zone. Structurally, the warhead integrates multiple subsystems to ensure functionality and safety (**Figures 45** and **46**). The main assembly comprises a cylindrical casing (casing 1: aluminum, 0.6 kg, outer diameter: 198 mm, internal diameter: 196 mm; casing 2: aluminum, 2.1 kg, outer diameter: 122.5 mm, internal diameter: 110.5 mm) filled with RDX and encased by spherical fragments. An internal spring-loaded piston mechanism, calibrated for a chamber pressure of approximately 60 atmospheres, serves as part of the detonation triggering system, facilitating controlled initiation upon explosive activation. The initiation system employs three asymmetrically arranged initiators, which offer an optimal balance between cost, system simplicity, and effectiveness. This configuration also takes advantage of the warhead's cylindrical symmetry to achieve high percentages of both fragment impact probability and explosive energy utilization. The number of fragments required to effectively destroy the intended target was determined to be approximately 5953. This value ensures sufficient coverage and lethality within a 10-m engagement range. The directional nature of the warhead allows for remote control selection of the optimal detonation direction, significantly increasing operational flexibility. The overall design is compliant with the warhead's mass limitation of 20 km and meets all performance expectations, including the required lethal radius. The detonation system includes three EFI-type initiators, which are electrically fired and directionally arranged to create a focused fragmentation pattern (**Figure 47a**). Activation of the warhead is governed by a G-switch safety system (**Figure 47b**), which ensures arming only occurs within a specific acceleration range, typically between 50 gr and 300 gr (thickness: 1 mm, long: 15 mm, width: 50 mm). The G-switch and related safety components are assembled to comply with strict mechanical tolerances to prevent premature initiation. The design ensures a consistent fragmentation density along the warhead's length, yielding 49 fragments per unit length and a total of 2730 spherical projectiles per warhead ring configuration. The internal components, including the piston, spring, and initiator housing, are arranged to maintain the structural integrity of the warhead while minimizing its dimensions. The overall geometry and component distribution are optimized to maintain a total warhead mass of 20 km and provide a 10-m effective engagement range. The relevant critical geometrical, assembly, and performance data are presented in the Appendix.

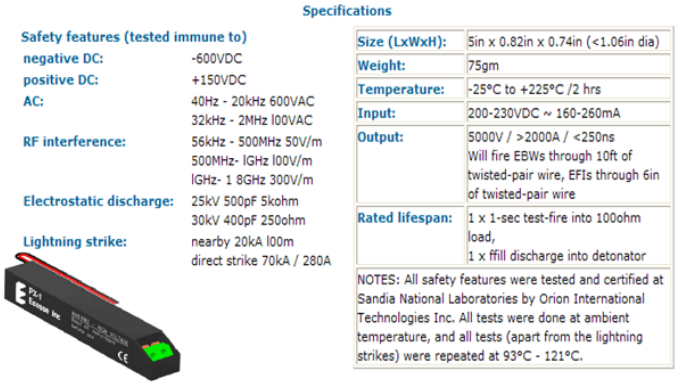

Specifications

Safety features (tested immune to)	
negative DC:	-600VDC
positive DC:	+150VDC
AC:	40Hz - 20kHz 600VAC 32kHz - 2MHz l00VAC
RF interference:	56kHz - 500MHz 50V/m 500MHz- lGHz l00V/m lGHz- 1 8GHz 300V/m
Electrostatic discharge:	25kV 500pF 5kohm 30kV 400pF 250ohm
Lightning strike:	nearby 20kA l00m direct strike 70kA / 280A

Size (LxWxH):	5in x 0.82in x 0.74in (<1.06in dia)
Weight:	75gm
Temperature:	-25°C to +225°C /2 hrs
Input:	200-230VDC ~ 160-260mA
Output:	5000V / >2000A / <250ns Will fire EBWs through 10ft of twisted-pair wire, EFIs through 6in of twisted-pair wire
Rated lifespan:	1 x 1-sec test-fire into 100ohm load, 1 x ffill discharge into detonator

NOTES: All safety features were tested and certified at Sandia National Laboratories by Orion International Technologies Inc. All tests were done at ambient temperature, and all tests (apart from the lightning strikes) were repeated at 93°C - 121°C.

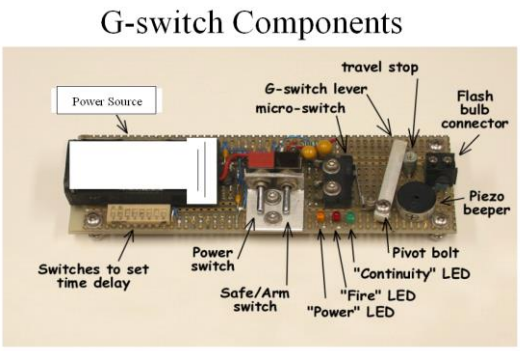

(a) **(b)**

Figure 47. Initiator activation components: **(a)** EFI (directional) detonator view and data. **(b)** G-switch components assembly.

11. Stealth and camouflage strategies for missile and aerial systems

Effective anti-interception and camouflage strategies for missile systems incorporate physical, thermal, and electromagnetic concealment techniques. A common method involves employing high-energy propellants that generate large, particle-rich exhaust plumes contaminated with varying particle sizes and smoke, resembling aircraft countermeasures such as chaff dispensers [42–52]. Reducing missile dimensions also contributes to decreased detectability.

Complementary to this approach is the use of energy-absorbing materials, which lower the thermal signature and reduce wake and plume visibility. In asymmetric configurations, thermal insulation materials are paired with alumina-based propellants to amplify the visible plume, providing a masking effect behind which the missile can conceal its trajectory. Furthermore, maneuverability is enhanced through thrust modulation, achieved by using composite cylindrical propellants with varying lengths, widths, or types, enabling real-time adjustments to acceleration, deceleration, and flight path, as depicted in **Figures 48** and **49**. The shape of the propellant grain—such as star-shaped or internally segmented geometries—also influences thrust patterns and guidance accuracy. In addition, splitting projectiles (**Figure 50**) and launching multiple warheads or shells—uniform or dispersed—are employed to overwhelm interception systems.

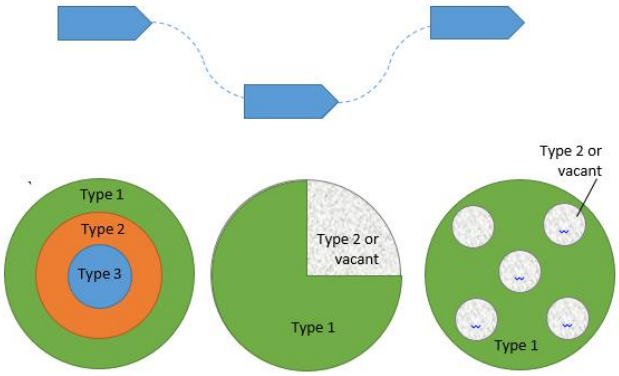

Figure 48. Projectile course dependency on propellant type and geometry.

Figure 49. Thrust magnitude (accelerating/decelerating) affected by motor pulses consisted of different propellant types and geometries.

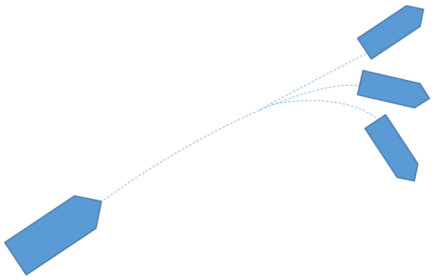

Figure 50. Projectile splitting illustration.

Stealth capabilities for UAVs, drones, and rotary-wing platforms depend on minimizing detectable signatures across five domains: field, geometry, visual, acoustic, and thermal [42–52]. Tactics include low-altitude, low-speed flight to reduce radar cross-section; using environmental features like clouds to obscure line-of-sight detection; and stationary or slow hover operations to avoid movement-triggered surveillance. Structurally, angular designs such as rhombus-shaped cuts in the body reflect radar waves away from the source [45–49]. Radar scattering is minimized through rhombus or conical shapes in the missile nose and optimized materials in the nozzle and combustion chamber that alter noise frequency and reduce signature [45–50]. Radar cross-section is further minimized using the relation $\sigma = \lambda^2/\pi G$, where λ is radar wavelength and G is a geometric constant. Visually, absorptive coatings made from carbon or rubber—often in dark tones like deep blue—reduce optical and radar reflectivity [53–58]. Propulsion systems can be enclosed or constructed with variable geometry to modulate and suppress acoustic emissions [50]. Heat is mitigated through lateral dissipation or by deploying survivability systems like chaff or decoy dispensers.

To achieve stealth for missile systems, the operational environment is manipulated into a masking domain using smoke generators and a multitude of decoys (e.g., artillery shells, simple UAVs). High-altitude, low-Mach flights help diminish heat and radar exposure. Staggered launches, separated by several seconds, reduce predictability and tracking reliability [42–45,50–52]. Adjusting the chemical composition of propellants also contributes to low-emission plumes [59,60].

Heat signature reduction is accomplished by distributing thermal output along the missile body and integrating ablative materials that efficiently absorb heat [61,62]. Radar Absorbent Materials (RAM) are fundamental to stealth, consisting of non-conductive materials such as polymers [53–55], carbon-fiber reinforced polymers [61,62], carbon nanotubes [57], and carbon-based dielectric composites [61]. Advanced RAM also includes multi-layer composites of thermoplastic polyurethane and carbon [63], polyurethane alone [64], polymer matrix composites [61,65,66], E-glass/epoxy [67–70], aerogels [71–73], and sandwich structures [74]. Conductive materials, such as composite honeycomb panels [75], nickel-coated glass/epoxy laminates [76], graphene-based composites [77,78], special metal mixtures [62,79–81], and metamaterials [82,83], have also demonstrated efficacy. Novel water-based coatings are emerging as viable options [84,85].

Color treatments, particularly in the deep blue spectrum, can offer radar-resilient characteristics. Over time, several stealth coatings have been patented [86,87], including carbon-based outer layers, anechoic rubber tiles, durable Styrofoam composites, and specialized paints.

In conclusion, modern anti-interception tactics integrate staggered volleys of diverse projectiles, each with unique velocities, sizes, and flight profiles, accompanied by exaggerated trails of hot gases and particles. When combined with environmental camouflage, plume manipulation, geometry-based radar scattering, and RAM coatings, these techniques significantly reduce detectability, making interception probabilities exceedingly low—typically below 5%.

12. SRM ground test and flight test

Prior to the flight test, a static ground firing was conducted, guided by methodologies and data of existing researches [24,34,35,59,88–104]. The design of the post-firing test stand facility was based on tested information [24,34,35,88–98], with all environmental and safety protocols implemented [59,88–99,104]. Spectrometric analysis of exhaust gases was performed, aligned with thrust measurements via load cells and chamber pressure diagnostics. The flight test encompassed telemetry-based trajectory tracking, canard servo performance validation, and an evaluation of target interception accuracy.

The flight test procedure included: Pre-test briefing; UAV launch; telemetry systems check; target alignment for verification ("White Test"); systems checkout; live missile launch; target recovery; missile debris retrieval; post-test debriefing.

Data Acquisition requirements: Radar tracking of target and missile trajectories (*x, y, z, t*), miss distance determination, high-speed imaging of interception, telemetry data: Missile acceleration data; missile navigation data; angle of attack; steering angles and commands; temperature readings (gauges); electric voltage levels.

Target's pilot checklist: (i) Pre-launch: Standard takeoff checklist. (ii) Flight conditions: (Velocity: 300 m/s (Mach 0.8); Height 20,000 ft); Key Events: Countdown and launch; Engagement and interception assessment; Performance reporting. Contingency (e.g., Hang Fire): Abort protocols initiated by the safety officer, project chief, or designated pilot. Post-Flight: Landing and post-landing procedures.

Test Range Configuration: Tracking Stations: Camera A: 35 mm film, 5 m focal length; Camera B: 70 mm film, 10 m focal length; Thermal and Theodolite Tracking: (i) Target: Eastern and southern stations (with radar). (ii) Missile: Northern station (with radar).

13. Comparative assessment: Horned-viper vs. representative interceptor missiles

The following **Table 12** provides a qualitative and quantitative comparison between the Horned-Viper configuration and several existing interceptor missile systems—X-90, AIM-120C-7, R-73, AIM-9 Sidewinder, and the Arrow missile [105]. The analysis considers key performance, structural, guidance, propulsion, and warhead parameters. Note that earlier type of interception systems were presented conceptually by Hartlage et al. [106] (air projectile) and Williams et al. [107] (guided interceptor), respectively.

Horned-Viper is conceived as a research-oriented technological demonstrator, integrating stealth, propulsion, guidance, and warhead technologies in a single interceptor design. Unlike the X-90 (a Cold War–era ground-launched supersonic missile) or the Arrow (an operational anti-ballistic interceptor), Horned-Viper focuses on mid-range engagements (60 km ± 10%) while maintaining a compact form (0.2 m diameter, 3–4 m length). In terms of speed and altitude, Horned-Viper reaches Mach 4.0, comparable to the AIM-120C-7, and exceeds the R-73 and Sidewinder (both Mach 2.5). Its ceiling—above 20 km—is on par with air-to-air interceptors but below the exo-atmospheric domain of the Arrow.

Table 12. Transmission versus motor parameters.

Parameter	Horned-Viper	X-90	AIM-120C-7	R-73	AIM-9 Sidewinder	Arrow (Israel)
Role	Technological demonstrator, multi-role	Strategic supersonic missile	Beyond-visual-range air-to-air	Short-range air-to-air	Short-range air-to-air	Anti-ballistic interceptor
Launch Mode	Air/Ground-to-Air	Ground-based	Air-launched	Air-launched	Air-launched	Ground-launched
Max Speed (Mach)	4.0	3.0–3.5	4.0	2.5	2.5	> 9.0
Range (km)	60 ± 10%	300–400	~105	~30	~35	> 90
Altitude Ceiling (km)	> 20	> 25	> 20	~15	~18	Exo-atmospheric (> 100)
Max Load Factor (g)	30	~15	30	12	10–12	Not disclosed
Guidance Type	PNG + PID (full digital loop)	Inertial + terminal seeker	Active radar homing	IR homing	IR homing	Radar (active and semi-active)
Control System	Canard + freely rotating tail + PID	Tail fins only	Tail fins + TVC	Thrust vector + tail fins	Tail fins + IR seeker	Aerodynamic + TVC
Warhead Type	Directional frag, dual-pulse	Conventional HE	High-explosive blast frag	High-explosive frag	High-explosive frag	Directed fragmentation
Warhead Weight (kg)	20	~100	~18–23	~8	~9–10	~70–90
RCS Reduction Features	Stealth-optimized inlet + blended canards	None	Low observability (shaped)	None	Limited (IR only)	Not stealth-optimized
Propulsion Type	2-stage solid, dual-pulse	Liquid (scramjet variants)	Solid	Solid	Solid	Solid
Actuation Technology	Electric servo + miter gear	Pneumatic/Hydraulic	Electric	Mechanical/TV	Electric	Hydraulic + electro-mech
Stabilization Method	Fin + canard + spin	In-flight stabilization	Control fins	Aerodynamic + TVC	Aerodynamic fins	Inertial + aerodynamic
Sensor Fusion	IMU + potential IR/Radar seeker	Minimal	Inertial + active radar	IR only	IR only	Radar + IR + inertial
Simulation Validation	CFD + 6-DOF + PID model	Partial (classified)	Extensive field testing	Operational field-tested	Operational field-tested	Extensive testing
Developmental Status	Conceptual demonstrator	Cold War prototype	Fully deployed	Fully deployed	Fully deployed	Operation

Aerodynamically, Horned-Viper achieves sustained 10 g turns at Mach 1.5, a 20%–30 % improvement in agility over the AIM-120C-7's control surfaces and markedly higher than the R-73 (12 g) or Sidewinder (10–12 g). This performance derives from blended canards and a dual-horn inlet, which not only enhance lift but also reduce frontal radar cross-section by 45% compared to conventional inlets. Neither the R-73 nor the Sidewinder incorporates such stealth shaping, nor do the AIM-120C-7 and X-90 only employ limited contouring. The Horned-Viper's two-stage dual-pulse solid motor delivers a total impulse of 538.6 kN·s, allowing thrust modulation during midcourse and terminal phases—an advantage over single-pulse solid motors in the AIM-120C-7, R-73, and Sidewinder. While the X-90 may use scramjet or ramjet sustainers for extended range, that approach increases complexity and airframe volume. The Arrow also uses staged solids but for exo-atmospheric flight. Guidance is managed by proportional navigation with a PID loop, producing a 10 Hz

closed-loop bandwidth. Under identical test conditions, Horned-Viper's guidance and control yield a 12% faster intercept than the AIM-120C-7. In contrast, the AIM-120C-7 relies on an active radar seeker with tailfin/TVC control, and the R-73 or Sidewinder uses infrared seekers without closed-loop PID tuning, resulting in slower terminal convergence.

Its warhead employs directional spherical fragments (about 5953 steel balls), producing a 10 m lethal radius and a 15% increase in fragment effectiveness versus conventional ring-wound warheads of similar mass (18–23 kg in AIM-120C-7 or 8–10 kg in R-73/Sidewinder). The X-90's much heavier warhead (~100 kg) is designed for blast rather than focused fragmentation, and the Arrow uses a kinetic kill vehicle. Structurally, Horned-Viper's airframe (≈ 90 kg empty plus 20 kg warhead) is built from maraging steel, aluminum alloys, and ceramics to balance strength, weight, and thermal resistance. This matches the AIM-120C-7's overall weight but with a smaller cross-sectional area (0.031 m^2). By comparison, the R-73 and Sidewinder are lighter (40–50 kg total) but less stealthy and less agile at high Mach. The X-90 and Arrow are substantially heavier, reflecting their longer-range mission sets.

In summary, Horned-Viper's combination of a stealth-optimized airframe, dual-pulse propulsion, high-g canard control, rapid PID-guidance loop, and directional fragmentation warhead produces a demonstrator that outperforms or matches existing air-to-air interceptors in agility, stealth, and lethality within its intended mid-range, supersonic envelope.

14. Conclusions

Interceptor missile development has historically occurred in separate academic and operational realms, with student projects often focusing on individual subsystems and military programs making incremental upgrades to legacy designs. In response to the absence of an integrated demonstrator, the Horned-Viper project serves as a technological demonstrator aimed at validating and integrating advanced design features—such as stealth-optimized geometrical shaping, dual-pulse (solid-propellant) propulsion, agile (high-deflection canard) control surfaces, and a directional spherical-fragmentation warhead—into a unified interceptor platform. While grounded in academic methodology, the project advances toward operational relevance through detailed simulations and planned experimental validation. High-fidelity CFD and six-degree-of-freedom simulations have confirmed that the dual-horn inlet reduces frontal RCS by 45%, while the two-stage, dual-pulse motor provides a total impulse of 538.6 kN·s and sustains 10 g maneuvers at Mach 1.5. A PID-tuned guidance loop achieves a 10 Hz closed-loop bandwidth, shortening time-to-kill by 12% relative to an AIM-120C-7 equivalent scenario. The warhead's optimized spherical fragments deliver a 10 m lethal radius, improving fragment impact probability by 15% over traditional designs. In sum, Horned-Viper demonstrates that these integrated technologies can meet or exceed the performance of existing interceptors—such as the AIM-120C-7, R-73, Sidewinder, X-90, and Arrow—within a 60 km engagement envelope. Future work will focus on wind-tunnel RCS validation, servo bench tests, and subscale flight trials to mature this concept toward a full-scale prototype.

At present, current essay does not include any physical test data; all results are

based on high-fidelity CFD, 6-DOF trajectory simulations, and PID-model validation. Future work will focus on wind-tunnel RCS validation, servo bench tests, and subscale flight trials to mature this concept toward a full-scale prototype.

Conflict of interest: The author declares no conflict of interest.

Abbreviations

6-DOF	Six Degrees of Freedom
CAD	Computer-Aided Design
CFD	Computational Fluid Dynamics
CG	Center of Gravity
CoP	Center of Pressure
CoG	Center of Gravity
FEA	Finite Element Analysis
GNC	Guidance, Navigation, and Control
IMU	Inertial Measurement Unit
IR	Infrared
L/D	Lift-to-Drag Ratio
LOAL	Lock-On After Launch
MDO	Multidisciplinary Design Optimization
PID	Proportional–Integral–Derivative (control)
RCS	Reaction Control System

References

1. Fitzpatrick MJ. A case study in weapons acquisition: The Sidewinder Air-to-air Missile. Journal of International Affairs. 1985; 39(1): 175–190.
2. Basciano T. Sounding rocket flight experiment for undergraduates. In: Proceedings of the 36th AIAA Aerospace Sciences Meeting and Exhibit; 1998.
3. Bouchez M. High speed propulsion - A 10 years AEROSPATIALE-MATRA education contribution. In: Proceedings of the 9th International Space Planes and Hypersonic Systems and Technologies Conference; 1999.
4. Akins B, Frederick R. Undergraduate Propulsion Laboratory Projects at UAH. In: Proceedings of the 39th AIAA/ASME/SAE/ASEE Joint Propulsion Conference and Exhibit; 2003.
5. Paul S, Frederick R, Davis C. Advanced Tactical Missile. In: Proceedings of the 39th AIAA/ASME/SAE/ASEE Joint Propulsion Conference and Exhibit; 2003.
6. Neu J, Williams B, Collicott S, et al. Flight of the Redbird 10-H. In: Proceedings of the 39th AIAA/ASME/SAE/ASEE Joint Propulsion Conference and Exhibit; 2003.
7. Foster W, Hartfield R, Jenkins R. University Propulsion Programs at Auburn University. In: Proceedings of the 40th AIAA/ASME/SAE/ASEE Joint Propulsion Conference and Exhibit; 2004.
8. Dubois J, Lafrance P, Lestage R, et al. High Energy Missile Project. ADM001736. In: Proceedings of the Army Science Conference (24th); 2005.
9. Dyer J, Doran E, Dunn Z, et al. Design and Development of a 100km Nitrous Oxide/Paraffin Hybrid Rocket Vehicle. In: Proceedings of the 43rd AIAA/ASME/SAE/ASEE Joint Propulsion Conference & Exhibit; 2007.
10. Grosse M, Schlatzke G. Development of a Hybrid Rocket Motor Using a Diaphragm for a Small Test Rocket. In: Proceedings of the 44th AIAA/ASME/SAE/ASEE Joint Propulsion Conference & Exhibit; 2008.
11. Tsohas J, Appel B, Rettenmaier A, et al. Development and Launch of the Purdue Hybrid Rocket Technology Demonstrator. In: Proceedings of the 45th AIAA/ASME/SAE/ASEE Joint Propulsion Conference & Exhibit; 2009.

12. Collins K, Burt A, Moser M. A Student Approach to Rocket Design. In: Proceedings of the 46th AIAA/ASME/SAE/ASEE Joint Propulsion Conference & Exhibit; 2010.
13. Ronningen JE, Berger M, Vesterås R. Development of a Student Hybrid Rocket. In: Proceedings of the 48th AIAA/ASME/SAE/ASEE Joint Propulsion Conference & Exhibit; 2012.
14. Tran PHN, Booth MJ, Robinson JH, et al. Development and Test of an Experimental Hybrid Sounding Rocket. In: Proceedings of the 8th Intercollegiate Rocket Engineering Competition; 2013.
15. Okninski A, Marciniak B, Bartkowiak B, et al. Development of the Polish Small Sounding Rocket Program. Acta Astronautica. 2015; 108: 46–56. doi: 10.1016/j.actaastro.2014.12.001
16. Nicholson S, Pietz G, Pointer J, Whitmore J. Development of an experimental hybrid rocket: CSU IREC Team. In: Proceedings of the 2015 COSGC Research Symposium; 2015.
17. Apel U, Baumann A, Dierken C, et al. AQUASONIC – A Sounding Rocket Based on Hybrid Propulsion. Applied Mechanics and Materials. 2016; 831: 3–13. doi: 10.4028/www.scientific.net/amm.831.3
18. Lestrade J-Y, Messineo J, Hijlkema J, et al. Hybrid Chemical Engines: Recent Advances from Sounding Rocket Propulsion and Vision for Spacecraft Propulsion. AerospaceLab Journal. 2016; 11: 1–14. doi: 10.12762/2016.AL11-14
19. Bach C, Sieder J, Weig F, Tajmar M. Development of a Liquid-Propellant Student Sounding Rocket. In: Proceedings of the 65th German Aerospace Congress (DGLR); 2016.
20. Okninski A, Kindracki J, Wolanski P. Rocket rotating detonation engine flight demonstrator. Aircraft Engineering and Aerospace Technology. 2016; 88(4): 480–491. doi: 10.1108/aeat-07-2014-0106
21. Ganesh M, Nandini C, Reddy MR, et al. Modeling and analysis of outer shell of cruise missile. International Journal of Research in Engineering and Technology. 2016; 05(03): 270–274. doi: 10.15623/ijret.2016.0503053
22. Nowakowski P, Okninski A, Pakosz M, et al. Development of small solid rocket boosters for the ILR-33 sounding rocket. Acta Astronautica. 2017; 138: 374–383. doi: 10.1016/j.actaastro.2017.06.007
23. Dutta A, Ernst Z, Buddhavarapu S, et al. The Yellow Jacket Space Program: Insights into Starting a Student Led Space-Shot Rocketry Team at the Georgia Institute of Technology. In: Proceedings of the AIAA Scitech 2019 Forum; 2019.
24. Heeg F, Kilzer L, Seitz R, et al. Design and Test of a Student Hybrid Rocket Engine with an External Carbon Fiber Composite Structure. Aerospace. 2020; 7(5): 57. doi: 10.3390/aerospace7050057
25. Nagineni A, Deepika AU. Design and Analysis of Missile Nozzle. IOP Conference Series: Materials Science and Engineering. 2018; 455: 012016. doi: 10.1088/1757-899x/455/1/012016
26. Perelstein Y, Sofer I, Rapoport Y, et al. “SELA” - Supersonic engine at low altitude. In: Proceedings of the 44th Israel Annual conference on Aerospace Sciences; 2004.
27. Sivan O, Eliav R, Alosh O, et al. CANAAN - Medium Range Cruise Missile. In: Proceedings of the 39th Israel Annual conference on Aerospace Sciences; 2009.
28. Technion - Israel Institute of Technology. The Horned Viper Project: Medium Range Anti-Aircraft Missile. Technion - Israel Institute of Technology; 2010.
29. Kogan A, Arochas B, Gafni G, et al. The Sky Fox Ramjet. In: Proceedings of the 52nd Israel Annual conference on Aerospace Sciences; 2012.
30. Achache Y, Ben-Uri E, Nevo B, et al. “Parash” - Anti-Tank Missile. In: Proceedings of the 54th Israel Annual conference on Aerospace Sciences; 2014.
31. Krishnan S. Hybrid Rocket Technology: An Overview. In: Proceedings of the 6th Asia Pacific International Symposium on Combustion and Energy Utilization; 2002.
32. Caveny LH, Geisler RL, Ellis RA, et al. Solid Rocket Enabling Technologies and Milestones in the United States. Journal of Propulsion and Power. 2003; 19(6): 1038–1066. doi: 10.2514/2.6944
33. Okninski A. On use of hybrid rocket propulsion for suborbital vehicles. Acta Astronautica. 2018; 145: 1–10. doi: 10.1016/j.actaastro.2018.01.027
34. Vernacchia MT, Mathesius KJ, Hansman RJ. Low-Thrust Solid Rocket Motors for Small, Fast Aircraft Propulsion: Design and Development. Journal of Propulsion and Power. 2022; 38(1): 122–134. doi: 10.2514/1.b38104
35. Alazeezi M. Design and optimization of dual-propellant grains of solid rocket motors [PhD thesis]. Belgrade (RS): University of Belgrade; 2024.
36. Douglas HW, Collins JH Jr. NASA Space Vehicles Design Criteria: Solid Rocket Motor Igniters. NASA SP-8051; 1971.

37. Nakka R. Experimental Rocketry Web Site: Igniter System. Available online: www.nakka-rocketry.net/paradigm.html (accessed on 2 June 2025).
38. PacSci EMC. Rocket Motor Igniter. Available online: psemc.com/products/pyro-igniters/ (accessed on 2 June 2025).
39. Defence Research and Development Organisation (DRDO). Ignition System for Solid Rocket Motors. Technology Focus. 2020; 28(1).
40. Natali M, Rallini M, Torre L, et al. High Temperature Composites from Renewable Resources: A Perspective on Current Technological Challenges for the Manufacturing of Non-Oil Based High Char Yield Matrices and Carbon Fibers. Frontiers in Materials. 2022; 9. doi: 10.3389/fmats.2022.805131
41. Nagler J. On Thermoelastic Impact Modelling of Frozen Composite Target During Pre – Heated Projectile Penetration Starts of Motion. PROOF. 2024; 4: 26–68. doi: 10.37394/232020.2024.4.4
42. Ousborne DR. Influence of radar stealth technology on the penetration ability of anti-ship missile. fohns Hopkins APL Technical Digest. 1993; 14(2): 125–140.
43. Serdar C. RF stealth (or low observable) and counter-RF stealth technologies: Implications of counter-RF stealth solutions for Turkish Air Force [Master's thesis]. Monterey (CA): Naval Postgraduate School; 2009.
44. Wu Q, Zheng B, Zhang G, et al. Intelligent Reflecting Surface-Aided Electromagnetic Stealth Over Extended Regions. IEEE Wireless Communications Letters. 2025; 14(6): 1628–1632. doi: 10.1109/lwc.2025.3549892
45. Xiong X, Zheng B, Swindlehurst AL, et al. A New Intelligent Reflecting Surface-Aided Electromagnetic Stealth Strategy. IEEE Wireless Communications Letters. 2024; 13(5): 1498–1502. doi: 10.1109/lwc.2024.3378455
46. Lomazzi L, Cadini F, Giglio M, et al. Vulnerability assessment to projectiles: Approach definition and application to helicopter platforms. Defence Technology. 2022; 18(9): 1523–1537. doi: 10.1016/j.dt.2021.09.001
47. Zheng B, Xiong X, Tang J, et al. Intelligent Reflecting Surface-Aided Electromagnetic Stealth Against Radar Detection. IEEE Transactions on Signal Processing. 2024; 72: 3438–3452. doi: 10.1109/tsp.2024.3420149
48. Grant RA. The radar game. AIR FORCE Magazine; 1999.
49. Shin H, Yoon D, Kim C, et al. Shape Optimization of an Integrated Mast for RCS Reduction of a Stealth Naval Vessel. Applied Sciences. 2021; 11(6): 2819. doi: 10.3390/app11062819
50. Gong J, Yan J, Kong D, et al. Radar detection of wake vortex behind the aircraft: the detection range problem. ARXIV; 2023.
51. Yadav VK, Bansal P, Sharma S. A review of stealth technology. International Journal of Trend in Scientific Research and Development. 2020; 4: 719–722.
52. Староверов (RU) НЕ, Староверов НЕ. Anti-helicopter and anti-stealth missile. RU2443968C2, 19 March 2009.
53. Shirke N, Ghase V, Jamdar V. Recent advances in stealth coating. Polymer Bulletin. 2024; 81(11): 9389–9418. doi: 10.1007/s00289-024-05166-4
54. Balaji Ananth P, Abhiram N, Hari Krishna K, et al. Synthesis of radar absorption material for stealth application. Materials Today: Proceedings. 2021; 47: 4872–4878. doi: 10.1016/j.matpr.2021.06.196
55. Danesh M, Beheshti H, Heidari-Rarani M. Optimal design of broadband radar-absorbing composite structures based on different compositions, processing, and geometric parameters. Journal of Reinforced Plastics and Composites. 2022; 42(9-10): 430–445. doi: 10.1177/07316844221129694
56. Kim S, Lee S, Zhang Y, et al. Carbon-Based Radar Absorbing Materials toward Stealth Technologies. Advanced Science. 2023; 10(32). doi: 10.1002/advs.202303104
57. Kolanowska A, Janas D, Herman AP, et al. From blackness to invisibility – Carbon nanotubes role in the attenuation of and shielding from radio waves for stealth technology. Carbon. 2018; 126: 31–52. doi: 10.1016/j.carbon.2017.09.078
58. Hu J, Hu Y, Ye Y, et al. Unique applications of carbon materials in infrared stealth: A review. Chemical Engineering Journal. 2023; 452: 139147. doi: 10.1016/j.cej.2022.139147
59. Ecker T, Karl S, Hannemann K. Combustion Modeling in Solid Rocket Motor Plumes. In: Proceedings of the 8th European Conference for Aeronautics and Space Sciences Madrid, Spain; 2019.
60. Okninski A, Kopacz W, Kaniewski D, et al. Hybrid rocket propulsion technology for space transportation revisited - propellant solutions and challenges. FirePhysChem. 2021; 1(4): 260–271. doi: 10.1016/j.fpc.2021.11.015
61. Pan Z, Han S, Wang J, et al. Polyimide fabric-reinforced polyimide matrix composites with excellent thermal, mechanical, and dielectric properties. High Performance Polymers. 2020; 32(10): 1085–1093. doi: 10.1177/0954008320928387

62. Wang L, Xu G, Liu C, et al. Surface-modified CeO2 coating with excellent thermal shock resistance performance and low infrared emissivity at high temperature. Surface and Coatings Technology. 2019; 357: 559–66.
63. Kasgoz A, Korkmaz M, Durmus A. Compositional and structural design of thermoplastic polyurethane/carbon based single and multi-layer composite sheets for high-performance X-band microwave absorbing applications. Polymer. 2019; 180: 121672. doi: 10.1016/j.polymer.2019.121672
64. Zhang W, Zhuang Y, Zhang J, et al. Preparation and performance control of ultra-low near-infrared reflectivity coatings with super-hydrophobic and outstanding mechanical properties. Scientific Reports. 2024; 14(1). doi: 10.1038/s41598-024-71164-1
65. Ahmad H, Tariq A, Shehzad A, et al. Stealth technology: Methods and composite materials—A review. Polymer Composites. 2019; 40(12): 4457–4472. doi: 10.1002/pc.25311
66. Jayalakshmi CG, Inamdar A, Anand A, et al. Polymer matrix composites as broadband radar absorbing structures for stealth aircrafts. Journal of Applied Polymer Science. 2018; 136(14). doi: 10.1002/app.47241
67. Kim PC, Lee DG. Improvement of Bonding Characteristics Between the Frequency Selective Surface and E-Glass/Epoxy Composites for Stealth Radomes. Journal of Adhesion Science and Technology. 2009; 23(2): 215–227. doi: 10.1163/156856108x369570
68. Kurniawan AF, Anwar MS, Nadiyyah K, et al. Thickness optimization of a triple-layered microwave absorber combining magnetic and dielectric particles. Asia-Pacific Journal of Science and Technology. 2025; 30(2).
69. Silva TI, Pontes Soares K, Miranda Pereira I, et al. Evaluation of Epoxy Resin Composites in Multilayer Structure for Stealth Technology. Journal of Aerospace Technology and Management. 2020; (1): 37–40. doi: 10.5028/jatm.etmq.23
70. Zhang J, Zhang W, Guan Q, et al. Preparation and Properties of Epoxy Resin and Polyurethane Blend Resin-Based Low-Infrared-Emissivity Coatings. Coatings. 2022; 12(11): 1708. doi: 10.3390/coatings12111708
71. Sun H, Yang B, Ji D, et al. Bioinspired aerogels: ingenious structure, remarkable performance, and versatile applications. Journal of Materials Chemistry A. 2024; 12(21): 12358–12380. doi: 10.1039/d4ta00851k
72. Zhou J, Chen Y, Li H, et al. Facile synthesis of three-dimensional lightweight nitrogen-doped graphene aerogel with excellent electromagnetic wave absorption properties. Journal of Materials Science. 2017; 53(6): 4067–4077. doi: 10.1007/s10853-017-1838-3
73. Shi T, Zheng Z, Liu H, et al. Configuration of Multifunctional Polyimide/Graphene/Fe3O4 Hybrid Aerogel-Based Phase-Change Composite Films for Electromagnetic and Infrared Bi-Stealth. Nanomaterials. 2021; 11(11): 3038. doi: 10.3390/nano11113038
74. Xu R, Wang W, Yu D. A novel multilayer sandwich fabric-based composite material for infrared stealth and super thermal insulation protection. Composite Structures. 2019; 212: 58–65. doi: 10.1016/j.compstruct.2019.01.032
75. Choi JH, Jang MS, Jang WH, et al. Investigation on microwave absorption characteristics of conductive-coated honeycomb absorber. Composite Structures. 2020; 242: 112129. doi: 10.1016/j.compstruct.2020.112129
76. Kwak BS, Choi WH, Noh YH, et al. Nickel-coated glass/epoxy honeycomb sandwich composite for broadband RCS reduction. Composites Part B: Engineering. 2020; 191: 107952. doi: 10.1016/j.compositesb.2020.107952
77. Huang Z, Chen H, Xu S, et al. Graphene-Based Composites Combining Both Excellent Terahertz Shielding and Stealth Performance. Advanced Optical Materials. 2018; 6(23). doi: 10.1002/adom.201801165
78. Youh MJ, Huang YR, Peng CH, et al. Using Graphene-Based Composite Materials to Boost Anti-Corrosion and Infrared-Stealth Performance of Epoxy Coatings. Nanomaterials. 2021; 11(6): 1603. doi: 10.3390/nano11061603
79. Chai X, Zhu D, Chen Q, et al. Tailored composition of low emissivity top layer for lightweight visible light-infrared-radar multiband compatible stealth coating. Advanced Composites and Hybrid Materials. 2022; 5(4): 3094–3103. doi: 10.1007/s42114-022-00563-7
80. Benitha VS, Jeyasubramanian K, Prabhin VS. Enhanced near-infrared reflectance and functional characteristics of nano metal oxide embedded alkyd coatings. Materials Research Express. 2022; 9(5): 056404. doi: 10.1088/2053-1591/ac6fbd
81. Li X, Li M, Li X, et al. Low Infrared Emissivity and Strong Stealth of Ti-Based MXenes. Research. 2022; 2022. doi: 10.34133/2022/9892628
82. Dubey A, Shami TC. Metamaterials in electromagnetic wave absorbers. Defence Science Journal. 2012; 62: 261–8.
83. Shi M, Xu C, Yang Z, et al. Achieving good infrared-radar compatible stealth property on metamaterial-based absorber by controlling the floating rate of Al type infrared coating. Journal of Alloys and Compounds. 2018; 764: 314–322. doi: 10.1016/j.jallcom.2018.06.093

84. Liu ZH, Ban GD, Ye ST, et al. Infrared emissivity properties of infrared stealth coatings prepared by water-based technologies. Optical Materials Express. 2016; 6(12): 3716. doi: 10.1364/ome.6.003716
85. Yan X, Wang L, Qian X. Preparation and Characterization of Low Infrared Emissive Aluminum/Waterborne Acrylic Coatings. Coatings. 2020; 10(1): 35. doi: 10.3390/coatings10010035
86. Cui J, Ma Y, Yang B, et al. Infrared stealth coating and preparation method thereof. CN102417771B, 28 September 2011.
87. Qu Q, Weng X, Xie J, et al. Method for coating infrared stealth coating on object surface coated with radar absorbing coating. CN103980806A, 22 May 2014.
88. NASA. Captive-fired testing of solid rocket motors. NASA; 1971.
89. Fry RS. Solid propellant test motor scaling. CPIA; 2001.
90. Tengli PN. A study on vibration problems of solid propellant rocket motor [Master's thesis]. India: Dr. M.G.R. Educational and Research Institute University; 2011.
91. Tengli PN, Ramesh CS, Viswanathan K, Saravanan R. Frequency analysis of instability observed in a large segmented solid rocket motor. Indian Journal of Science and Research. 2012; 65.
92. Freeman CW II. Solid rocket motor static fire test stand optimization: load cell effects and other uncertainties [Master's thesis]. Huntsville (AL): The University of Alabama in Huntsville; 2018.
93. Ünal A, Yaman K, Okur E, et al. Design and Implementation of a Thrust Vector Control (TVC) Test System. Journal of Polytechnic. 2018; 21(2): 497–505. doi: 10.2339/politeknik.404009
94. Waugh L, Moore E, Macfarlane J, et al. Overview of rocket testing at the Westcott test facility (2016/2017). In: Proceedings of the Space Propulsion Conference 2018; 2018.
95. McFarland M, Antunes E. Small-Scale Static Fire Tests of 3D Printing Hybrid Rocket Fuel Grains Produced from Different Materials. Aerospace. 2019; 6(7): 81. doi: 10.3390/aerospace6070081
96. Taherinezhad R, Zarepour G, Tabatabayee SS. Evaluation of Failure Factors of a Small-Scale Motor in Laboratory Testing. Journal of Failure Analysis and Prevention. 2020; 20(3): 617–626. doi: 10.1007/s11668-020-00878-x
97. Meghavath AR. Design of a state-of-the-art test facility for rocket engines [Master's thesis]. Sweden: School of Aerospace, Transport and Manufacturing, Astronautics and Space Engineering (Spacemaster); 2022.
98. Fernandes FAC, Souto C d'Andrade, Pirk R. Static Firing Tests of Solid Propellant Rocket Motors: Uncertainty Levels of Thrust Measurements. Journal of Aerospace Technology and Management. 2022; 14. doi: 10.1590/jatm.v14.1270
99. NASA. Environmental impact statement: Space Shuttle Program. Washington, D.C.; 1978.
100. Dawbarn R, Kinslow M. ARNOLD Engineering Development Center: studies of the exhaust products from solid propellant rocket motors. Report No.: ADA029569. Available online: https://ntrs.nasa.gov/api/citations/19770011266/downloads/19770011266.pdf (accessed on 2 June 2025).
101. Office of NEPA Policy and Compliance. DOE/EIS-0281: Draft Environmental Impact Statement (April 1999). Office of NEPA Policy and Compliance; 1999.
102. Ruffino P, Dimarzo M. The Effect of Evaporative Cooling on The Activation Time of Fire Sprinklers. Fire Safety Science. 2003; 7: 481–492. doi: 10.3801/iafss.fss.7-481
103. Test Operations at Arnold Engineering Development Center. Final of environmental assessment. Report No.: ADA611271. Available online: https://archive.org/details/DTIC_ADA611271 (accessed on 2 June 2025).
104. Yilmaz N, Vigil F, Height J, et al. Rocket motor exhaust thermal environment characterization. Measurement. 2018; 122: 312–319. doi: 10.1016/j.measurement.2018.03.039
105. Pecht E, Tishler A, Weingold N. On the choice of multi-task R&D defense projects: A case study of the Israeli missile defense system. Defence and Peace Economics. 2013; 24(5): 429–448. doi: 10.1080/10242694.2012.717205
106. Hartlage B, Owen M, Frederick R, et al. Enhanced Counter Air Projectile. In: Proceedings of the 40th AIAA/ASME/SAE/ASEE Joint Propulsion Conference and Exhibit; 2004. doi: 10.2514/6.2004-4086
107. Williams J, Brekke K, Patrick S, et al. Conceptual Design of a Guided Interceptor. In: Proceedings of the 41st AIAA/ASME/SAE/ASEE Joint Propulsion Conference & Exhibit; 2005. doi: 10.2514/6.2005-3847

Appendix

Table A1—Summarizes the key parameters used in Israeli projects methodological development which influenced the methodical of current project (Introduction Section).

Table A2—Presents the pros and cons of prescribed guidance methods which influenced on the guidance method selection (Section 9).

Table A3—Exhibits pros and cons of different warhead configurations which influenced on the warhead final fragmentation design configuration selection (Section 10).

Table A4—Shows pros and cons of various initiation configurations (Section 10.1).

Table A5—Presents accurate main warhead components for the final configuration (Section 10).

Table A1. Israeli projects development comparison.

Ref.	Threat Scenario	LAW Missile Design Requirements:	Propulsion System Selection	Airframe Design	Weight Estimation	Materials Selection
[26]	Interceptor cruise missile with supersonic speed or small unmanned reconnaissance aircraft ("SELA").	$M_{max} = 1.5$ (se level) Engine cost: \$2000 per unit Endurance: 50 hr The motor is able to fly 500 km with *M* = 0.8 and later 300 km with *M* = 1.5 towards the target (back and forth).	At the design point: Thrust = 3788 N Mass flow = 11.2 kg/sec Fuel For M = 0.8: SFC < 1.3 kg/kgf · hr Off-design point (see in detail at [33])	Max. diameter: 0.3 m Max. length = 1.336 m The design includes two spool turbofans with a fan, a low-pressure compressor, and a low-pressure turbine installed on the inner shaft and a high-pressure centrifugal compressor and turbine installed on the outer shaft. Combustor design (Max. temperature 1220 K) is made of a liner, inner casing, outer casing, mixer, and diffuser. The turbine (Max. temperature 1625 K) is constructed from 53 blades with appropriate stator geometry of 40 blades and a disk.	Total weight: 1250 kg Fuel weight: 250 kg Payload weight: 200 kg Support system weight: 300 kg Engine support system weight: 30 kg	High pressure turbine is made of Silicon Nitride (Si_3N_4), 5% of Alumina (A_2O_3) and 2% of Y_2O_3 Fan, Low pressure and High-pressure compressor are made of: Ti_6Al_4V The combustor is made of Nimonic86
[27]	Air launched cruise homing maneuver missile carried by F-15 or F-16 called "CANAAN"	Max. Range: 300 km. Max. Height: 6.1 km. *M* range (subsonic): 0.4–0.9. Minimum Radar cross-section (RCS). The warhead will be able to penetrate a 2 m thick concrete wall. The basic guidance principle is that the missile knows where it is and where the target is located. It is guided towards the target using a simple Pure Pursuit guidance law (3DOF instead of 6DOF).	Payload (Warhead) diameter = 152 mm Payload length = 1130 mm Payload diameter = 152 mm Max. Takeoff thrust = 1820 N. Max. continuous thrust = 1590 N Max. H.P. shaft speed = 85,000 rpm Max. L.P. shaft speed = 33,000 rpm Dimensions: 40 mm × 850 mm Max. fuel consumption: 79 kg/hr	CEP: 5 km Three kinds of design were compared: Design A: Round cross section—It was chosen as a baseline comparison for the other designs. Design B: Elliptical Cross Section—The configuration was chosen to get the benefit of the lift created by the fuselage. The shape was chosen to have low RCS lines. **Design C** (selected): Flying wing—The configuration was tested for the possibility of an extra low RCS. *X*c.g. = 920.6 mm Max. lift coefficient = 2.5	Total Weight: 250 kg Engine weight = 27 kg Payload (Warhead) mass: 100 kg	

Table A1. (*Continued*).

Ref.	Threat Scenario	LAW Missile Design Requirements:	Propulsion System Selection	Airframe Design	Weight Estimation	Materials Selection
[29]	Ramjet powered air-to-air missile, called 'The Sky Fox Ramjet' (TSFR) carried by F-15 or F-16.	Max. M = 2.5 Max. Height = 9144 m Max. Maneuver acceleration of 10 g at 1.5 M. The missile accuracy range is 10 m.	Ramjet engine and a booster (rocket engine) with hexagonal star geometry grain. Phase transition: nozzle expansion, inlet opening, dropping of the inlet plugs, gas generator nozzle opening, and primal burning of the gas generator Cstar = 1350 m/sec Pc = 71.5 atm $\dot{r} = 12$ mm/sec	The Max. diameter is 200 mm at the thickest section and 150 mm at the thinnest section Total length = 0.36 m 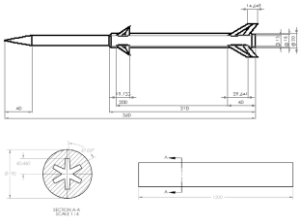 A directional warhead was designed with 7500 Tungsten fragments (each fragment has a 4.6 mm diameter). Fragments' velocity is 2500–3000 m/sec. A proximity fuse based on laser beam projection from 8 points on the missile's circumference.	Total weight: 165 kg Warhead weight: 20 kg. Propellant weight: 117 kg Nozzle and Servo weights: 5 kg Engine hose: 5 kg Nose weight: 4 kg. G&C weight: 12 kg	Warhead made of RDX, Tungsten Lugs are made of 4130 Steel Rudders are made of 7075 Al Engine hose is made of Marage Steel
[30]	Autonomous Anti-tank missile called 'Parash'	M = 0.6 Max. Range = 4100 m Min. Range = 50 m	Two solid rocket motors propel the "Parash" missile. The first one is the launch motor, which accelerates the missile to 30 m/s and finishes its operation while the missile is still in the canister. M7M propellant, with the Specific impulse of 246 s, is used for this task, shaped as 16 tubes, burning inside-out and outside-in at a rate of $\dot{r} = 35\ mm/s$ and generating chamber pressure of $Pc = 350\ atm$. Propellant mass is 0.116 kg, which stands for 22% of the total launch motor mass. Propellant of the main motor contains 87% AP and 13% HTPB, Cstar = 1508 m/s. Boost and Cruise data appear fully in [29].	Cruise: $\delta p{-}trim = -0.73°$ Maximum Maneuver: $\delta p{-}trim = -3.65°$ Tube diameter = 90 mm Max. Length = 1110 mm Canister square shape: 1.14 m × 0.11 m 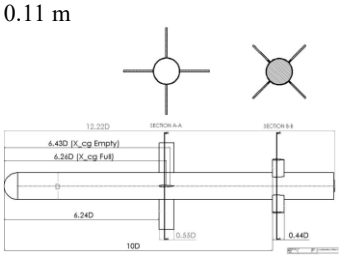 2.5 s acceleration of the missile from launch speed (30 m/s) to cruise speed (200 m/s). Up to 19 s of constant cruise speed. Guiding the missile to the target using proportional navigation. Warhead full details appear in [29].	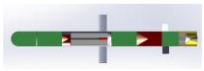 Total Weight = 12.71 kg Canister weight = 2.7 kg Tripod's weight = 7.7 kg	Casing: Al 2024-T3 Aerodynamic surface, Motor Casing: Al 7075-T6 Launch motor casing: 4340AISI steel, Normalized Canister & Tripod: Al 6063-T5 & Panex 33, Carbon Fiber - Epoxy

Table A2. Pros and cons of prescribed guidance methods.

Classical guidance methods (expansion)	Definition	Scheme	Advantages	Disadvantages
Command Line of Sight	O—Zero Point T—target M—Missile (Three points method)	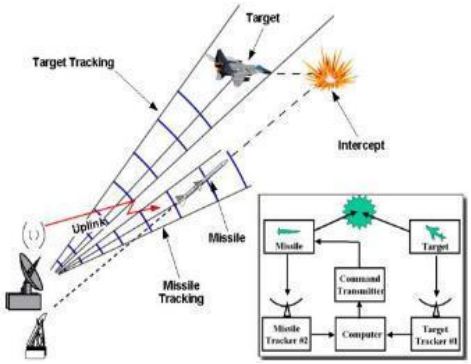 A guiding law that aspires to a geometric law that maintains the line of sight.	There is no need for an expensive homing head (the price of the missile).	Sensitivity to noise—low accuracy for long distances. Requires information transfer always to the missile.
Beam Riding Guidance	Same	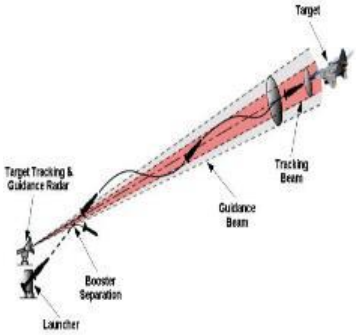 The missile “rides” directly on a beam directly to the missile from O. Types of rays: radio, infrared, a laser beam with a wavelength in the visible range.	A relatively uncomplicated control system. Does not require the transmission of commands to the missile	Sensitivity to the weather conditions—inability to function under poor visibility conditions. homing guidance body (nose/head) section dependency. Sensitivity to disturbances and disruptions of the beam. Expansive homing guidance body (nose/head) section.
Pure Pursuit (‘Dog chase’)	T – target M – Missile (Two points method)	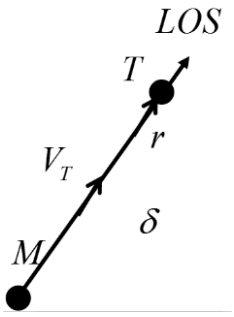 Two attitudes: Missile nose to the target/velocity vector to the target The missile aims to reach the rear of the target. A simple geometric rule: M follows independently and directly to T $\boxed{\vec{V}_M \times \vec{r} = 0}$	Velocity M is directed to the position of T.	Requires a homing guidance body (nose/head) section. Requires very large accelerations in the phase END GAME.
Proportional Navigation		Guidance law: command to change the rate of the body angle relative to the rate of change of the line of sight. A relative navigator requires a homing guidance head section that allows both tracking and measuring the rate of change of line of sight. The acceleration command is relative to the line of sight change. If the target is maneuvering, then at any moment the missile will acquire a new collision course, and hence acceleration will be required until the meeting/passing point. $\boxed{\dot{\gamma}_{M_c} = N\dot{\lambda} \; or \; a_{M_c} = k\dot{\lambda}}$	High accelerations are not required at the end of the interception	Electro-optic expansive homing guidance body (nose/head) section.

Table A3. Pros and cons of different warhead configurations.

The main prevalent warhead configurations	Advantages	Disadvantages	Sketch
Continuous-rod warhead	The rods exhibit elastic behavior, enabling them to deform and maintain integrity upon deployment. Any contact between the target and the expanding ring results in precise shearing of the impacted area.	The damage range is confined to the ring's diameter. Critical damage is ensured provided the ring remains intact and defect-free. The continuous rod design, with minimal fragmentation, limits the number of components capable of inflicting critical impact.	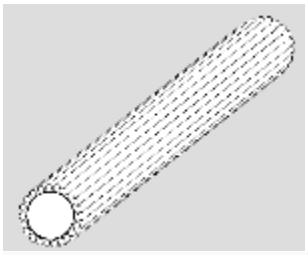 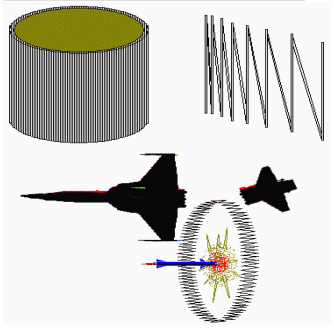 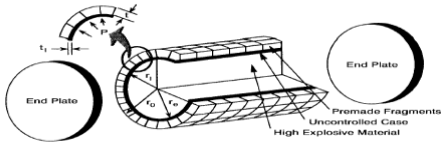 Figure 3.2. Premade fragments on uncontrolled fragmentation case
Rod warhead	The fragmented design yields a higher fragment count than continuous bars, enhancing coverage. While continuous rods inflict severe damage upon impact due to their mass, the discontinuous configuration offers a broader dispersion radius, improving overall lethality.	Rod directionality is difficult to control upon detonation, limiting targeting precision. Their shape increases aerodynamic drag, reducing velocity and effective range. Additionally, the larger size results in fewer fragments, decreasing overall hit probability.	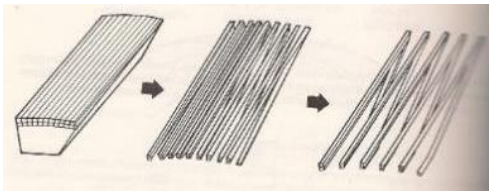 An optimized continuous rod warhead can be tailored to the missile's nose geometry, with cross-sectional shapes such as circular, trapezoidal, or square—typically around 5 mm^2 for velocities near 1 km/s. The payload forms an expanding annular ring of rods. While each rod possesses significantly greater inertia than spherical fragments, the reduced surface coverage limits overall effectiveness compared to fragment spray designs. Additionally, the rods' poor aerodynamic shape results in a narrow impact envelope, necessitating precise detonation timing for optimal performance.

Table A3. (*Continued*).

The main prevalent warhead configurations	Advantages	Disadvantages	Sketch
Balls warhead	$S_{ball} < S_{rod} < S_{continuity\text{-}rod}$: A high number of dispersed fragments increases the probability of critical damage across a broad area. Their smaller surface area results in lower aerodynamic drag, enhancing range and speed retention. This configuration allows for more controllable and directional dispersion compared to alternatives while also offering lower production costs and simpler manufacturing processes.	Owing to their small size, individual pellet balls inflict less damage per unit compared to single rods or continuous rod assemblies.	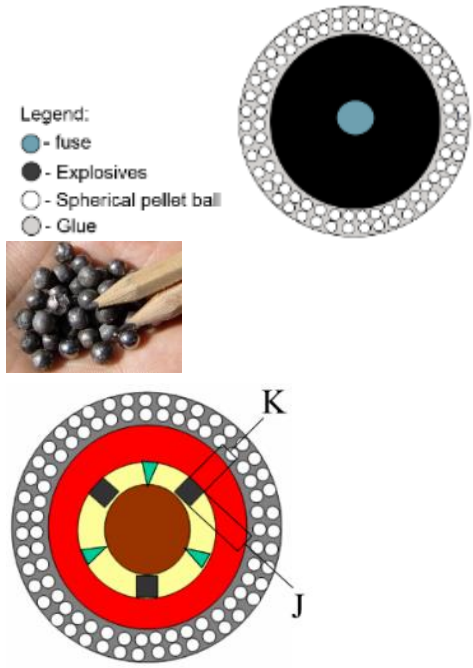 A typical spray-type warhead consists of a casing filled with closely packed spherical fragments arranged around an internal explosive core. 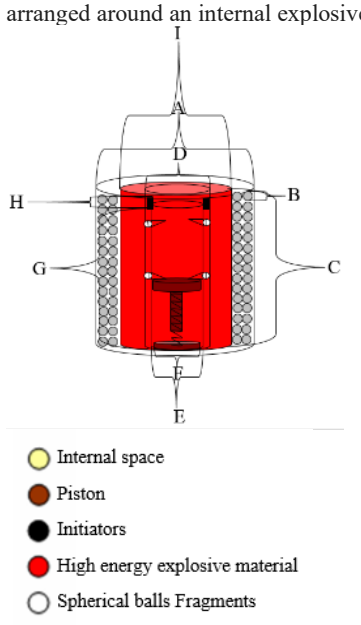

Table A4. Pros and cons of various initiation configurations.

Configuration	Cost [$]	Weight [kg]	Hit percentages of balls in relation to the effective high explosive material [%]	Percentage of use of the high effective explosive [%]	Hit probability as a function of the number of initiators in relation to the hit percentage of spheres in relation to the effective high explosive [%]	Number of actually hitting balls
Central initiator only 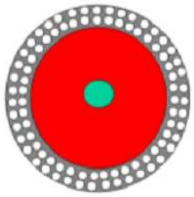	490	0.525	50	50	70	3010
Three symmetric initiators 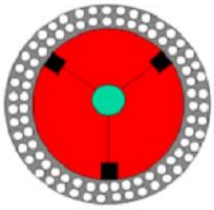	210	0.225	78.42	94.31	88.271	5953
Five symmetric initiators 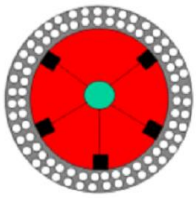	350	0.375	78.42	94.31	96.1	6480

Table A5. Accurate main warhead components geometry.

Measurement symbol [mm]	Meaning	Value
D1	Warhead diameter	198
D2	Casing 2 outer diameter	122.5
D3	Casing 2 internal diameter	28
D4	Ball diameter	7
H1	Warhead total length	350
H2	Total piston length	123
H3	Initiator location in relative to the warhead base	223